Exponent™
Failure Analysis Associates®

Exponent
310 Montgomery Street
Alexandria, VA 22314

telephone 703-549-9565
facsimile 703-549-4225
www.exponent.com

METALLURGICAL EVALUATION OF DOT-3AL-3000 CYLINDER J95119

Prepared for:

Research and Special Programs Administration
U.S. Department of Transportation
400 Seventh Street S.W.
Washington D.C. 20590

Prepared by:

Timothy R. Smith, Ph.D., P.E.
Carol E. Moyer

10/5/00

Reference No.: 957-6294
Project No.: DC18344.000
QA ID No.: DC18344.000/AOFO/1000/TS02

TABLE OF CONTENTS

LIST OF FIGURES

1.0 Introduction

The U.S. Department of Transportation (DOT) contracted with Exponent Failure Analysis Associates (FaAA) to perform a metallurgical examination of the remains of a failed aluminum SCUBA cylinder. The cylinder is a DOT-3AL-3000 type with serial number J95119 manufactured by Walter Kidde. The U.S. DOT seized the cylinder on March 18, 2000 in Key Largo, FL.

The scope of this investigation was to perform a detailed evaluation of the cylinder remains, including photodocumentation and non-destructive examinations, chemical analysis and mechanical property determination, metallographic sectioning and examination, and fractography. The detailed work scope for this evaluation is provided in Appendix A. This report presents the findings of this evaluation.

2.0 Visual Examination

A visual examination of the cylinder remains was performed. The remains are shown in Figures 1 and 2, in the as-received condition. The cylinder broke apart into three large pieces designated 1, 2, and 3 by FaAA, the tank valve, and several small fragments.

The "WK" stampings on the neck of the aluminum cylinder indicates that it was manufactured by Walter Kidde. Other stampings on the neck indicate that the first hydrostatic test on the cylinder was performed in 07/87, and this is taken as its date of manufacture. Inspection stampings indicate that the cylinder had been pressure re-tested in 05/93 and 06/98. A complete photodocumentation of the pieces was undertaken and is presented in Appendix B.

The fracture surfaces of the cylinder present on each of the three major fragments were inclined (i.e., non-radial with respect to the cylinder axis) shear-type, except in the neck region where the fracture surfaces were flat and radial with respect to the axis of the cylinder. The main fracture ran through essentially a full diameter of the inlet hole in the neck region. Figure 3 shows a photomontage of the fracture surface in the neck region.

Fragment 2, containing one-half of the neck region, sustained impact damage to its fracture surface and cylinder exterior, both likely as a result of the rupture event. Other pieces also showed impact damage and, at certain locations, scuffmarks. These also all appeared to be from the rupture event.

In the neck region, the inside wall of the cylinder showed multiple folds (or cusps) from the original manufacturing process (see Figure 4). The fracture surface on both sides of the inlet hole appeared to pass through folds of this type. On fragment 1 at least one crack, labeled C1 on Figure 4, was found originating from these folds.

3.0 Quantitative Chemical Analysis

Samples of chips from the neck of the cylinder, taken using an electric drill, were dissolved in solution and analyzed by inductively coupled plasma spectrometry (ICP) to determine chemical

composition. Samples of the cylinder neck and sidewall material were also analyzed by glow discharge mass spectrometry (GDMS) to determine trace levels of lead (Pb) and Bismuth (Bi). The GDMS technique was selected for its ability to detect trace level impurities in metals; however, it is less accurate than ICP for determining higher bulk levels. The results of these analyses are shown in Table 1; only the Pb and Bi results are shown for the GDMS. The bulk composition indicates that the cylinder material is consistent with the Aluminum Association (AA) 6351 alloy specification. These results also show compliance with the 1984 edition and the current edition of DOT federal regulation 49 CFR 178.46-5.

Table 1: Chemistry of the Cylinder

	Composition (wt.%)			
Element	Test Result Neck (ICP)	Test Result Neck (GDMS)	Test Result Sidewall (GDMS)	49 CFR-178.46-5 Specification
Mg	**0.59**	**-**	**-**	**0.40-0.80**
Si	**0.93**	**-**	**-**	**0.70-1.30**
Ti	**<0.02**	**-**	**-**	**0.20 max**
Mn	**0.43**	**-**	**-**	**0.40-0.80**
Fe	**0.17**	**-**	**-**	**0.50 max**
Cu	**<0.02**	**-**	**-**	**0.10 max**
Zn	**<0.03**	**-**	**-**	**0.20 max**
Bi	**<0.005**	**<0.000001**	**<0.00001**	**0.01 max**
Pb	**<0.01**	**0.00026**	**0.00036**	**0.01 max**
Al	**Balance**	**-**	**-**	**Balance**

Using this technique, the Pb-content was determined to be less than 4 weight-ppm. The bismuth (Bi) level was found to be below 0.1 weight-ppm.

4.0 Mechanical Testing

Tensile Testing

Full thickness tensile test coupons from the cylinder wall, aligned along the cylinder axis, were tested at room temperature in accordance with ASTM B 557 and following the procedure given by 49 CFR 178.46-13[1]. Samples were machined from Fragment 1 (Figure 1), from material showing minimal damage from the rupture event. The results of these tests are shown in Table 2.

The average strength values found are well above the current 49 CFR 178.46-5 minimum specification, but the measured elongation was found to be slightly below the minimum elongation requirements. The lower elongation values are likely attributable to natural aging of the material during service. They compare well with values of 42.8 ksi yield strength, 49.3 ksi

[1] The DOT 3AL specification requires tensile test specimens, representing a cylinder lot, to be taken in pairs oriented 180 degrees apart. In these tests, three specimens, taken adjacent to one another, were tested to preserve as much of the cylinder remains as possible. The balance of test protocol used, however, followed the procedure described in 49 CFR 178.46-13.

ultimate strength and 13% elongation (2 inch gauge length), published for AA6351 in T6 temper [1]. The DOT 3AL specification requires that the material be AA6351-T6.

Table 2: Mechanical Properties

Test	Yield (ksi)	UTS (ksi)	Elongation (%)	49 CFR 178.46-5 Yield (min.) (ksi)	49 CFR 178.46-5 UTS (min.) (ksi)	49 CFR 178.46-5 Elongation (min.) (%)
1-2-1	**49.0**	**54.1**	**11.8**	**37.0**	**42.0**	**14**
1-2-2	**48.6**	**53.2**	**14.3**	**37.0**	**42.0**	**14**
1-2-3	**48.4**	**53.3**	**13.6**	**37.0**	**42.0**	**14**
Average	**48.7**	**53.5**	**13.2**	**37.0**	**42.0**	**14**

Notes:
1. Tests were performed in accordance with the ASTM B 557 standard; gauge length was 2 inches.
2. Yield denotes the yield strength (0.2% offset), UTS denotes ultimate tensile strength.
3. Elongation values are from the flat coupons whereas the 49 CFR 178.46-5 requirements are based on cylindrical specimens.

Hardness Testing

Rockwell hardness measurements were made on a slice removed from the cylinder neck area. A total of six Rockwell B Scale measurements were taken using a Leco RT-370 Rockwell hardness tester; the results are shown in Table 3. It should be noted that the hardness measured perpendicular to the plane of fracture was slightly higher than that measured on a plane parallel to the fracture (66 RB vs. 63 RB). The observation reveals a possible effect of the as-formed texture on the strength properties.

Table 3: Hardness Measurements

Component	**Indent No.**	**Hardness (Rockwell B)**	**Average Hardness (Rockwell B)**
Neck, section oriented in plane of fracture	1	62.6	62.9 HRB
	2	63.8	
	3	62.2	
Neck, section oriented 90° to fracture (radial-circumferential)	4	65.2	66.2 HRB
	5	66.6	
	6	66.8	

5.0 Sectioning and Metallography

Figures 5 and 6 show the sections cut from cylinder fragment 1. Sections of the fracture surface on both sides of the inlet hole were cut such that the flat-faced portions of the fracture surface were separated from the fragment. Two wafers were generated in this process. Figure 6 also shows the further sectioning performed on fragment 1 from the neck region.

A section (1-1-3) was sliced in the neck region and then polished and etched to reveal its microstructure, Figure 7. The microstructure is typical for AA6351-T6 alloy [2]. The grain size is larger in the neck than the body and the grain size in the neck is relatively small, compared to the thickness at the neck. The majority of the grains in the neck region have a low grain aspect ratio (i.e., length and width are about the same).

Figure 8 shows section 1-1-6 (in the unetched and etched conditions) containing crack C1, taken parallel to the inlet hole just below the threads. Note the multiple folds at the inside surface and multiple cracks emanating from these folds. Figure 8b shows the section after preparation with a 1%HF+H_2O etch. The microstructure is typical for AA6351 in the T6 temper condition [2]. Note that the cracks emanating from the folds show fine-scale branches. The crack C1 shows a different character, with no branching, over the lower half of its extent (i.e., the portion furthest from the folds).

6.0 Fractography

The wafers containing the flat-faced fracture surface shown in Figure 5b (sections 1-1-1 and 1-1-2) were examined optically and in the scanning electron microscope (SEM). The optical examination revealed that the flat-faced region of the fracture surface showed little macroscopic ductility. Just outside of this region, the fracture surface transitioned to an inclined shear-type of fracture. The origin of the fractures appeared to be on each side of the inlet hole at folds (present at the time of manufacture) below the threads on the inside cylinder wall.

Fractography of the wafer also shows several beach marks in the flat-faced region, indicating progressive crack growth. Figure 9 shows an optical fractograph of section 1-1-1 (the lower fracture in Figure 3). Figures 10-12 show a series of SEM fractographs taken from this fracture surface in the flat-faced region at the locations identified in Figure 9.

Region A (SEM micrographs in Figure 10a) is near the inside of the cylinder, close to the threads at the inlet hole. Region B (SEM micrographs in Figure 10b) is close to the top of the inlet hole threads (Figure 9). Region C (SEM micrographs in Figure 10c) is near the outer cylinder wall. These three regions all contain predominantly intergranular fracture, with very fine-scale dimples on the faceted surfaces. Region D corresponds to a macroscopic beach mark and, at higher magnification (Figure 11), shows a relatively abrupt transition in failure mode from predominantly intergranular fracture to ductile rupture. This transition may be the result of a prior hydrostatic test. Between Regions D and E there is a progressive return to predominantly intergranular fracture, similar to Regions A, B and C. At Region E there is another relatively abrupt transition from predominantly intergranular fracture to predominantly ductile rupture, Figure 12. This region again corresponds to a macroscopic beach mark. The region beyond this beach mark shows predominantly dimpled rupture.

Figure 13 shows energy dispersive spectra (EDS) taken from the fracture surface. Region A is close to the origin area. Region B is in the darkened area near the top of the neck. Figure 13c shows the spectrum from the darkened region between Regions D and E (see Figure 9) with an overlay spectrum obtained from the region outside the beachmark furthest from the origin. The Cl, Na, O, P, and S peaks indicate the presence of corrosion product or contaminants.

Section 1-1-2 containing the upper flat-faced fracture surface shown in Figure 3, was also examined optically and in the SEM. As with Section 1-1-1, the flat-faced region of the fracture surface shows little macroscopic ductility and just outside of this region, transitions to an inclined shear-type of fracture. Figures 14-16 show the results of the fractographic examination of this section. Figure 14 is an optical micrograph showing beach marking, described earlier. A series of SEM fractographs were taken at the locations H and I of Figure 14. The SEM fractographs at these locations are shown in Figures 15 and 16.

Figure 17 shows energy dispersive spectra (EDS) taken from the fracture surface 1-1-2. Region F is close to the origin area and Region G is in the darkened area near the top of the neck. Figure 17c shows the spectrum from the darkened region at I (see Figure 14) with an overlay spectrum obtained from the region outside the beachmark furthest from the origin. The Na, O, P, and S peaks indicate corrosion product or contaminants.

Figure 18 shows SEM fractographs of the fracture surface from tensile specimen 1-2-1 used for mechanical property determination. The fracture surface consists primarily of ductile dimpled rupture, with both macro and micro dimples, and some intergranular faceting, with microdimpling on these facets. This morphology equates well to fracture surfaces generated by tensile and toughness testing [3] of other similar Al alloys.

7.0 Discussion

Examination and testing of the cylinder remains demonstrates that the subject cylinder meets the chemical property requirements of DOT 3AL specifications in the 1984 edition and the current DOT 49 CFR 178.46. Both lead (Pb) and bismuth (Bi) are below the regulation limits specified in 49 CFR 178.46-5. The cylinder alloy complies with the Aluminum Association specification for AA6351-T6 in accordance with DOT 3AL. The tensile elongation to failure, however, is slightly below the requirement of DOT 49 CFR 178.46. The microstructure appears to be typical for this alloy and heat treatment.

Fracture Mechanism

Examination of the fracture surfaces of each cylinder fragment suggests that the failure originated from the neck region of the cylinder at or very near the inlet hole. The region of fracture at the neck inlet hole was flat-faced and likely a result of sub-critical, time-dependent cracking. The sub-critical fracture process initiated on both diametrally-opposed sides of the inlet hole, growing to sufficient size to result in critical, time-independent fracture under certain pressurizing conditions. The cracks that developed on both sides of the inlet hole show very similar characteristics and appear to have grown by the same mechanism. The shape and

location of the beach marks on the fracture surface segments studied in detail suggests that the cracks propagated sub-critically (i.e., in a time-dependent manner) for the majority of the flat-faced region, with each beach mark representing a change in fracture process and loading condition. The presence of local ductile dimpling zones at each beach mark suggests changes from sub-critical cracking to critical cracking to crack arrest to resumption of sub-critical cracking, wherein the critical cracking phase is driven by a pressurization load. Such a pressurization load could correspond to a hydrotest event. The final phase of shear or slant-type fracture following the last beach mark nearest the outside surface of the cylinder represents the last-to-occur unstable fracture (rupture).

The beach marks and the overall character of the fracture surface in the neck region are consistent with the morphology of cracked neck regions of other DOT-specification and Australian-specification aluminum cylinders [4, 5, 11]. In addition, sectioning of the cylinder wall just below the threads at the inlet hole revealed multiple cracks from multiple origins at folds (or cusps) in the inside wall. These branched cracks are consistent with cracks found in the neck region of other DOT-6498, DOT-3Al, and DOT-7235 aluminum cylinders [4].

Since no fatigue striations or evidence of stress-corrosion cracking (SCC) were found, the observed cracks are more consistent with "sustained-load cracking" reported in the literature for similar Al alloys [3, 6-10] than with a fatigue or SCC sub-critical crack growth mechanism. This process continued up to the extent defined by the last beach mark on each side of the inlet hole. The fractures propagated from origins at the inside surface at the inlet hole and below the threads. The final rupture of the cylinder was a fast fracture event.

The neck crack, C1 (see Figures 4 and 8), showed a mechanical character (i.e., straight and non branched) in the deeper half of its extent. Although this crack was not forced open in the laboratory it is reasonable to assume, based on its extent parallel to the inlet hole, that it was not as deep as the flat regions on either main fracture surface. As such, the force required to extend this crack is expected to be much larger that that required to extend the main fracture. The mechanical character of the C1 crack segment is consistent with the fast fracture event that ruptured the cylinder being the result of a pressurization event.

Crack Length

Fractography suggests that cracks had initiated in the cylinder neck immediately below the threads, discussed above. Figures 19 and 20 show the crack surfaces at the neck with drawing overlays that correspond to the apparent maximum extent of sub-critical cracking. A measurement was taken from the postulated origin of each crack to the maximum extent of the blue lines shown in Figures 19 and 20 to establish crack length estimates. For the 1-1-1 fracture this estimate is 2.03 inches (51.7 mm) and for the 1-1-2 fracture this estimate is 1.74 inches (44.3 mm).

Time to Develop Cracking by SLC

A calculation was performed based on available SLC data from the literature (as described below) in order to estimate the time required to develop the extent of cracking observed.

The SLC mechanism is expected to be operative (at some location on the crack front) whenever the local mode I stress intensity factor, K_I, is above the threshold value necessary for detectable SLC advancement[2], but below the fracture toughness. If it is assumed that no significant periods of global arrest occur, an estimate of the minimum time for the cracks to grow is calculable through the use of average crack growth rates previously published (e.g., [6, 10]). To obtain an estimate of this minimum crack growth time, the highest mean propagation rate calculated from experiments by Stark and Ibrahim [10] is employed. This data set is used even though the Stark-Ibrahim material had a Pb-level of 100 ppm because no average growth rate data are available in the literature for a Pb-level closer to that measured for the subject cylinder. The use of 100 ppm Pb data for this analysis is expected to be conservative since it has been established that Pb-availability in the material is a critical factor for the SLC mechanism: the higher the Pb-level, the higher the crack propagation rate [4,6]. This estimate is also expected to be conservative because the incubation period for crack growth, as influenced by slow growth from an initial condition to the threshold crack-tip K_I condition, is ignored.

Measurement of the largest crack at the neck (Figure 17) results in a sub-critical crack extent or "length" of at least 51.7 mm. Using a mean propagation rate of 0.61×10^{-3} mm/hr [10], the time to develop the longest observed crack is estimated to be 9.7 years. A similar calculation performed for the other crack length results in an estimate of 8.3 years. These estimates are a significant fraction of the roughly 13 years that the cylinder was in service, following its first hydrostatic test in 1987.

These estimates of the time of cracking by SLC advancement (acting alone) are expected to be conservatively low but must be interpreted in the context of at least three other factors. First, the cylinder history is not fully known. Pressure variations due to overfilling (i.e., moderate overpressurization) or any exposure to elevated temperature could increase the crack propagation rate. Secondly, local variations in grain size, grain aspect ratio, and texture may have an effect on crack growth rate. The nature of this effect cannot be reliably predicted at this time. Thirdly, it is quite possible that crack advancement occurs during hydrotests as suggested by Price et al. [11]; this would be most likely at larger crack lengths. All of these factors are expected to influence the estimated time for the cracks to grow.

[2] Price et al. (1997) show that a threshold stress intensity of about 11 to 13 $MPa(m)^{1/2}$ likely exists based on their analysis of Lewandowski et al.'s data [6] and their observation that no growth has been shown in laboratory tests below 10 $MPa(m)^{1/2}$ [11]. Further simulation work suggests that the threshold stress intensity may be as low as 4 $MPa(m)^{1/2}$ [13]. Threshold behavior is known to occur for other subcritical growth mechanisms such as stress corrosion cracking (SCC); e.g., [12].

8.0 Summary and Conclusions

A metallurgical examination of a failed aluminum cylinder DOT-3AL-3000 type, with serial number J95119 showed the following results.

- This 1987-vintage cylinder meets the chemical requirements of the 3AL specification in 49 CFR 178.46-5 for AA6351 alloy, including lead (Pb) and bismuth (Bi) limits.

- This 1987-vintage cylinder meets the strength requirements of the 3AL specification in the 49 CFR 178.46-5, however the ductility is slightly below the specification.

- Multiple cracks with a multiple-branched morphology were found originating at folds in the interior wall in the neck region near the inlet hole. These folds were associated with the cylinder's manufacture.

- The cylinder failed from the neck region when sub-critical cracks in the neck region grew to critical size. The primary fracture surfaces developed from cracks at folds on the interior wall.

- The apparent origin of the fracture and mode of cracking are consistent with sustained-load cracks (SLC) reported in the literature for similar Al alloys. The crack size at the time of rupture appears to be defined by the macroscopic beach marks on the flat-faced (i.e., radial) portions of the fracture surface that were furthest away from the inlet hole.

- Estimates of the time-to-rupture, based on measurements of the crack lengths and on published crack-growth rate data, indicate that the neck cracks would have required at least 8 to 9 years prior to rupture to develop based on SLC propagation alone.

- The rupture of the cylinder is consistent with loading due to pressurization.

9.0 References

1. J. E. Hatch, Ed., (1984). Aluminum: Properties and Physical Metallurgy, American Society for Metals, Metals Park, OH, p. 363.

2. ASM Metals Handbook, 9th. Ed., Vol. 9, "Metallography and Microstructures", American Society for Metals, Metals Park, OH, p. 367.

3. M. Guttmann, B. Quantin, and Ph. Dumoulin (1983). "Intergranular creep embrittlement by non-soluble impurity: Pb precipitation hardened Al-Mg-Si alloys", Metal Sci., Vol. 17, No. 3, pp. 123-140.

4. J. H. Smith (1987). "Evaluation of Cracking in Aluminum Cylinders", NBSIR 86-3492, Institute for Materials Science and Engineering, National Bureau of Standards (NBS), U.S. Dept. of Commerce, Gaithersburg, MD.

5. J. W. H. Price, R. N. Ibrahim and D. Ischenko (1996). "Cracking in Aluminum 6061 and 6351 Gas Cylinders", Proc. Int. Conf. on Pressure Vessel Technology, Vol 1., American Society of Mechanical Engineers (ASME), Montreal, Canada, pp. 337-343.

6. J. J. Lewandowski, Y. S. Kim, and N. J. H. Holroyd (1992). "Lead-Induced Solid Metal Embrittlement of an Excess Silicon Al-Mg-Si Alloy at Temperatures of -4ºC to 80º C", *Met. Trans. A*., Vol. 23A, pp. 1679-1689.

7. Y. S. Kim, N. J. H. Holroyd, and J. J. Lewandowski (1989). "Pb-Induced Solid-Metal Embrittlement of Al-Mg-Si Alloy at Ambient Temperatures", *Proc. Environment-Induced Cracking of Metals*, National Association of Corrosion Engineers (NACE), pp. 371-377.

8. J. J. Lewandowski, V. Kohler, and N. J. H. Holroyd (1987). "Effects of Lead on the Sustained-load Cracking of Al-Mg-Si Alloys at Ambient Temperatures", *Mat. Sci & Eng*., Vol. 96, pp. 185-195.

9. H. L. Stark and R. N. Ibrahim (1992). "Crack Propagation in Aluminum Gas Cylinder Neck Material at Constant Load and Room Temperature", Eng. Fracture Mechanics, Vol. 41, No. 4, pp. 569-575.

10. H. L. Stark and R. N. Ibrahim (1988). "Crack Propagation at Constant Load and Room Temperature in an Extruded Aluminum", Eng. Fracture Mechanics, Vol. 30, No. 3, pp. 409-414.

11. J. W. H. Price, R. N. Ibrahim and D. Ischenko (1997). "Sustained Load Crack Growth Leading to Failure in Aluminum Gas Cylinders in Traffic", Engineering Failure Analysis, Vol. 4, No. 4, pp. 259-270.

12. J. M. Barsom and S. T. Rolfe (1987). Fracture and Fatigue Control in Structures, 2nd. Ed., Prentice-Hall, Inc., Englewood Cliffs, NJ, p. 347.

13. P. M. Singh, N.J.H. Holroyd, J. J. Lewandowski and J. T. Evans (1992). "Monte-Carlo Simulation of Lead Induced Slow Crack Growth in Al-Mg-Si Alloys", Parkins Symposium on Fundamental Aspects of Stress Corrosion Cracking, Edited by S. M. Bruemmer, E.I. Meletia, R. H. Jones, W. W. Gerberich, F. P. Ford and R. W. Stanchle, The Minerals Metals & Materials Society (TMS), pp. 567-583.

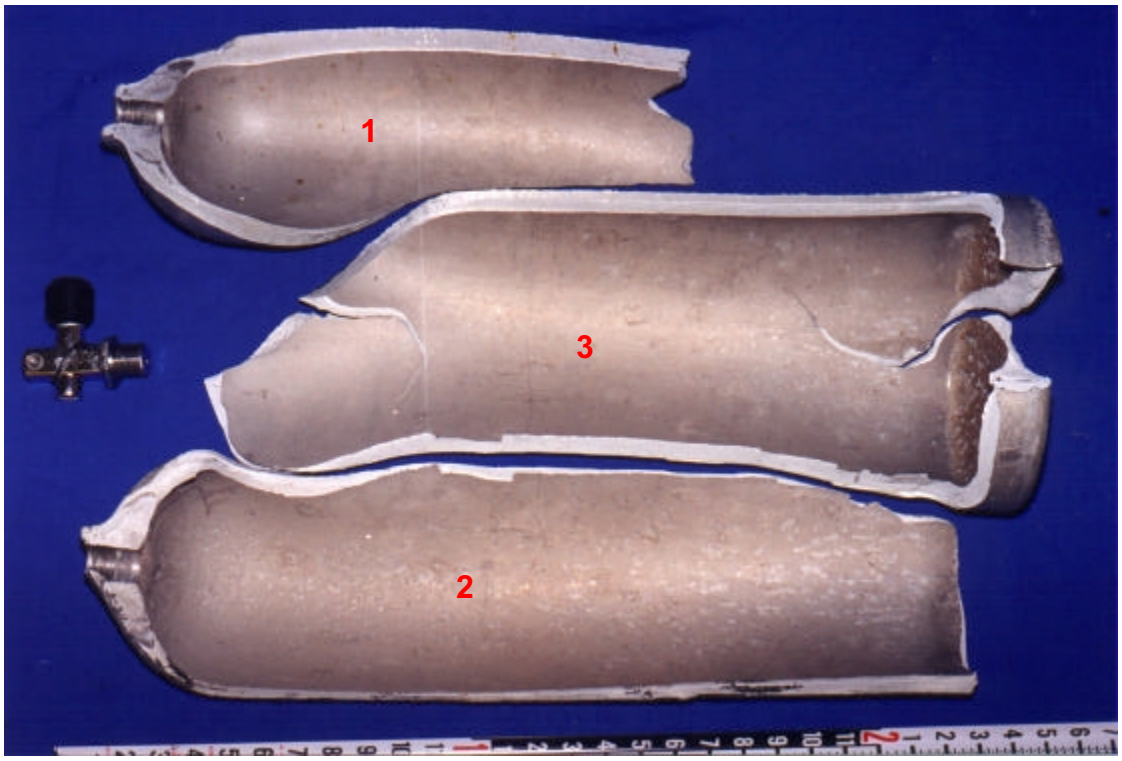

Figure 1. Cylinder remains, as received, showing fracture surfaces. Photo ID: DC18344-R4E4.

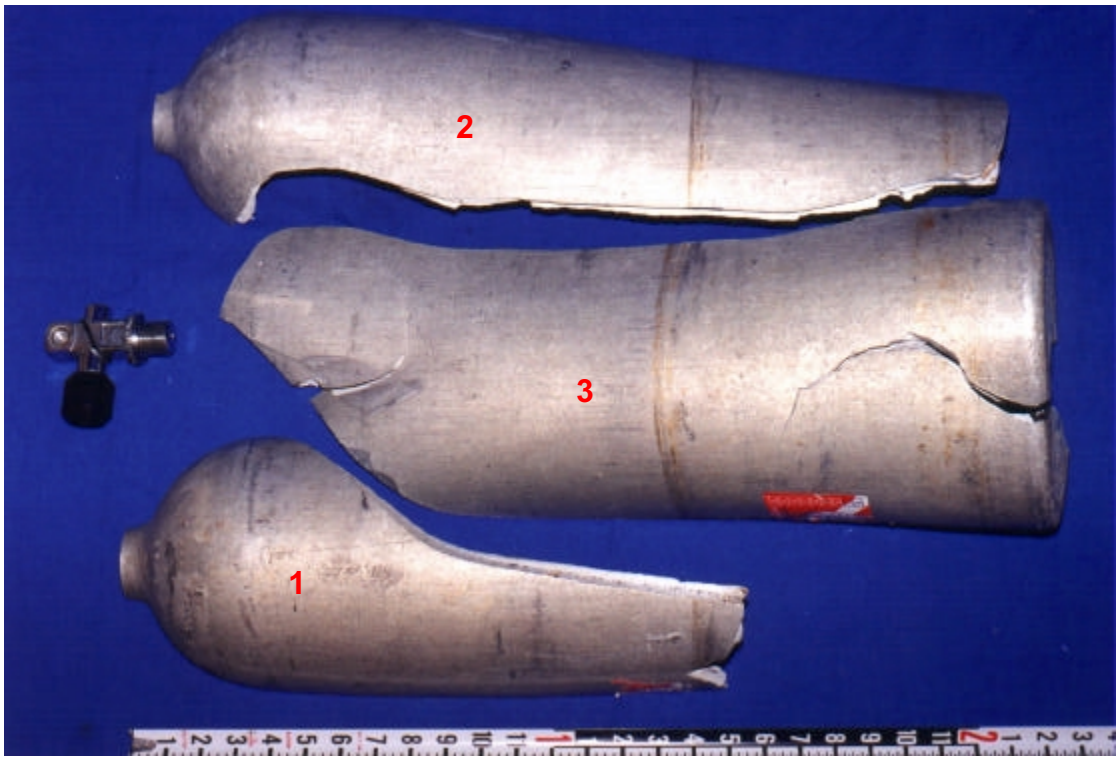

Figure 2. Cylinder remains, as received. Photo ID: DC18344-R4E45.

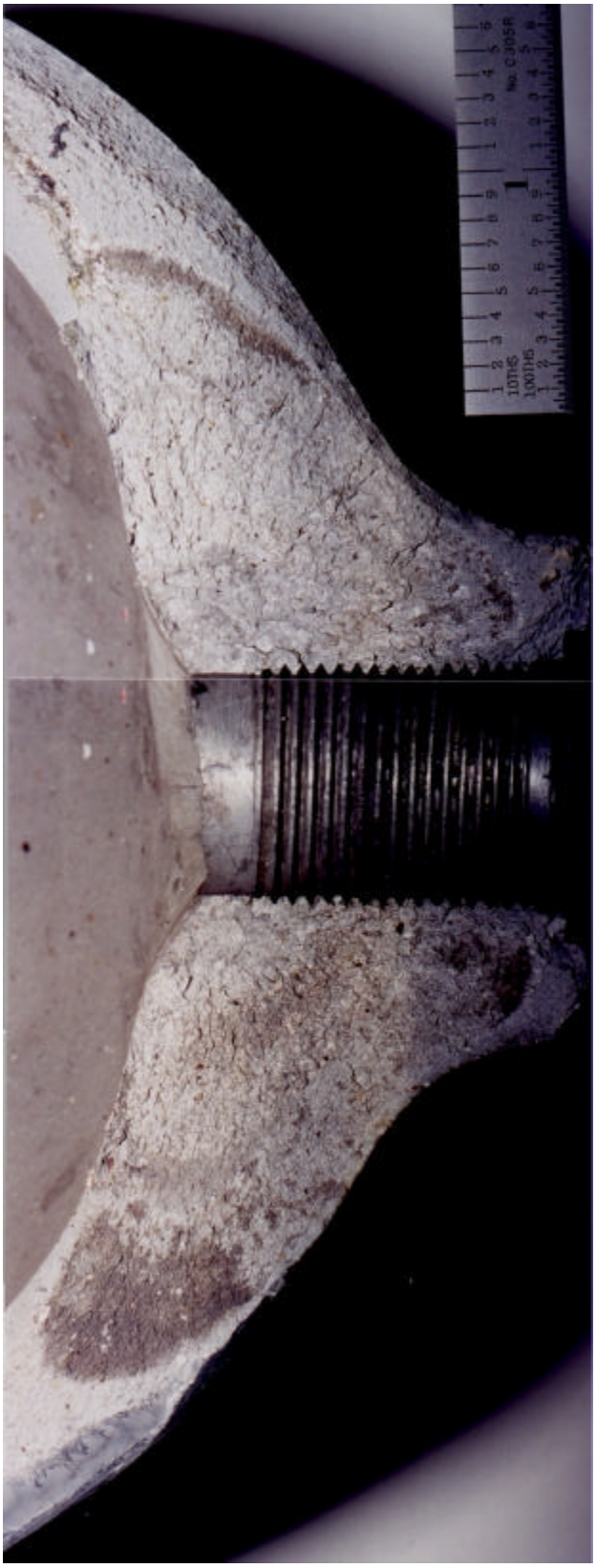

Figure 3. Photomontage of the fracture surface in the neck region. Photo ID: DC18344-R6E14,15.

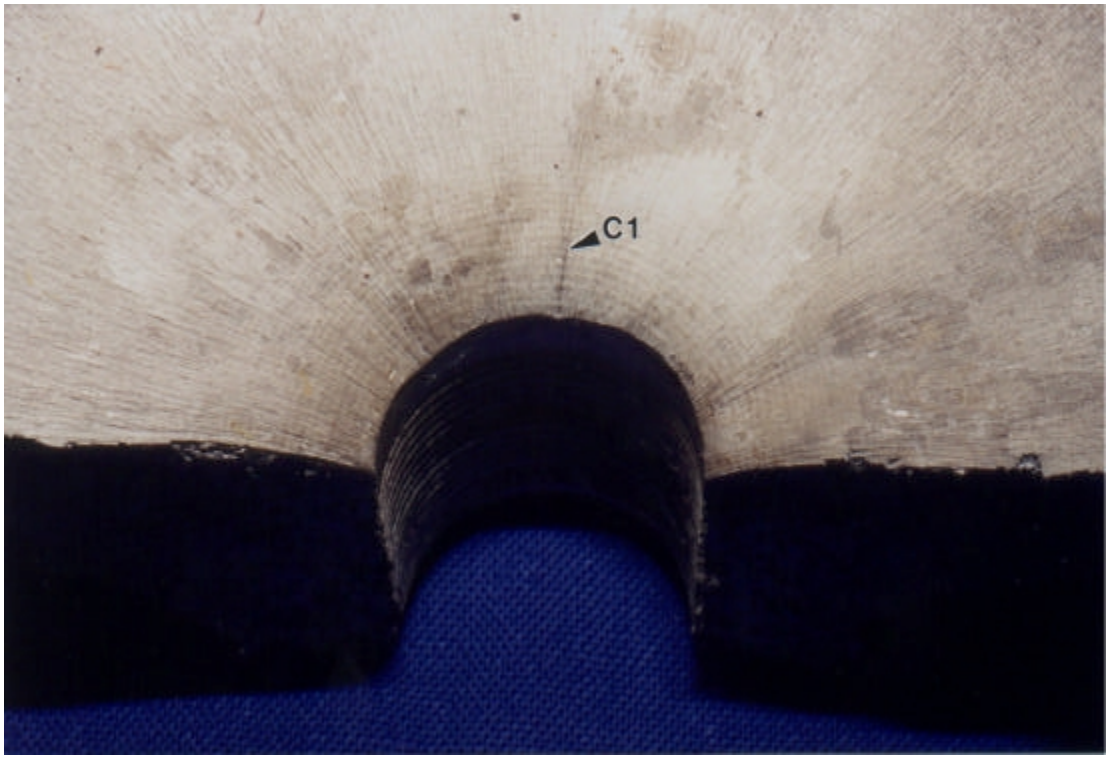

Figure 4. Close up of inside of the neck. A crack emanating from a neck fold is shown at C1. Photo ID: DC18344-R4E20.

(a)

(b)

Figure 5. Sectioning of fragment 1.
(a) Cut separating neck region. Photo ID: DC18344-R8E6.
(b) Sectioning of the neck region. Photo ID: DC18344-R10E4.

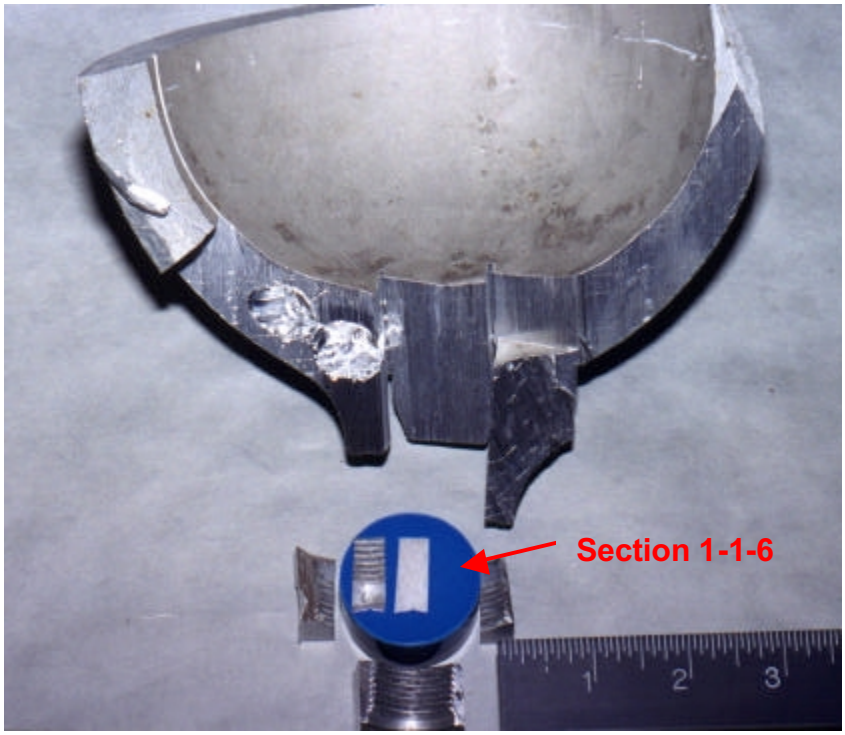

Figure 6. Further sectioning of fragment 1. Photo ID: DC18344-RE.

Figure 7. Microstructure of the neck region. Photo ID: DC18344-PAL-4,5,6-8/30/00.

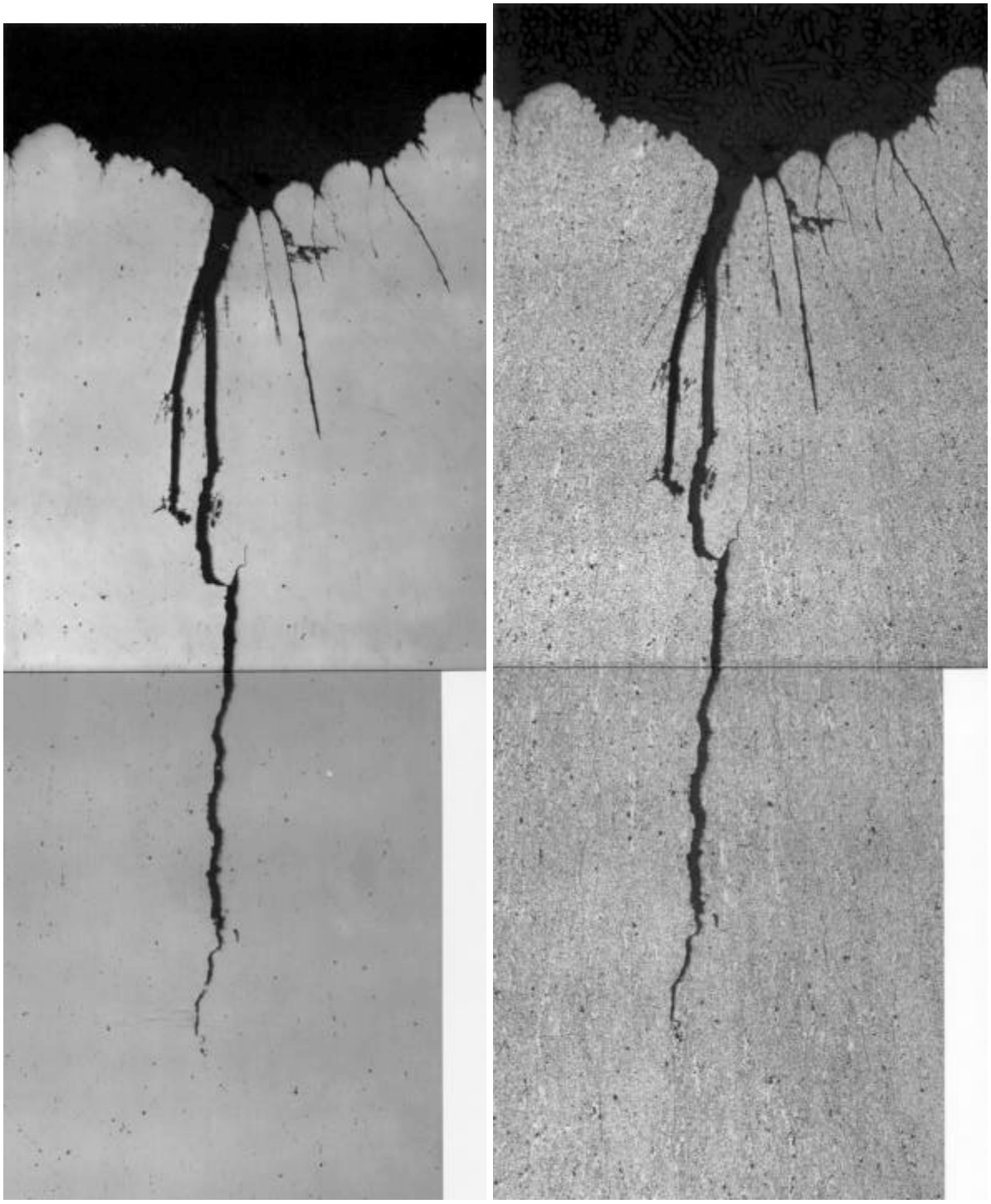

(a) (b)

Figure 8. Micrographs of crack C1 in the neck region. 100X.
(a) Unetched. Photo ID: DC18344-PAL-2,3-9/11/00.
(b) Etched 1% HF (aqueous). Photo ID: DC18344-PAL-4,5-9/11/00.

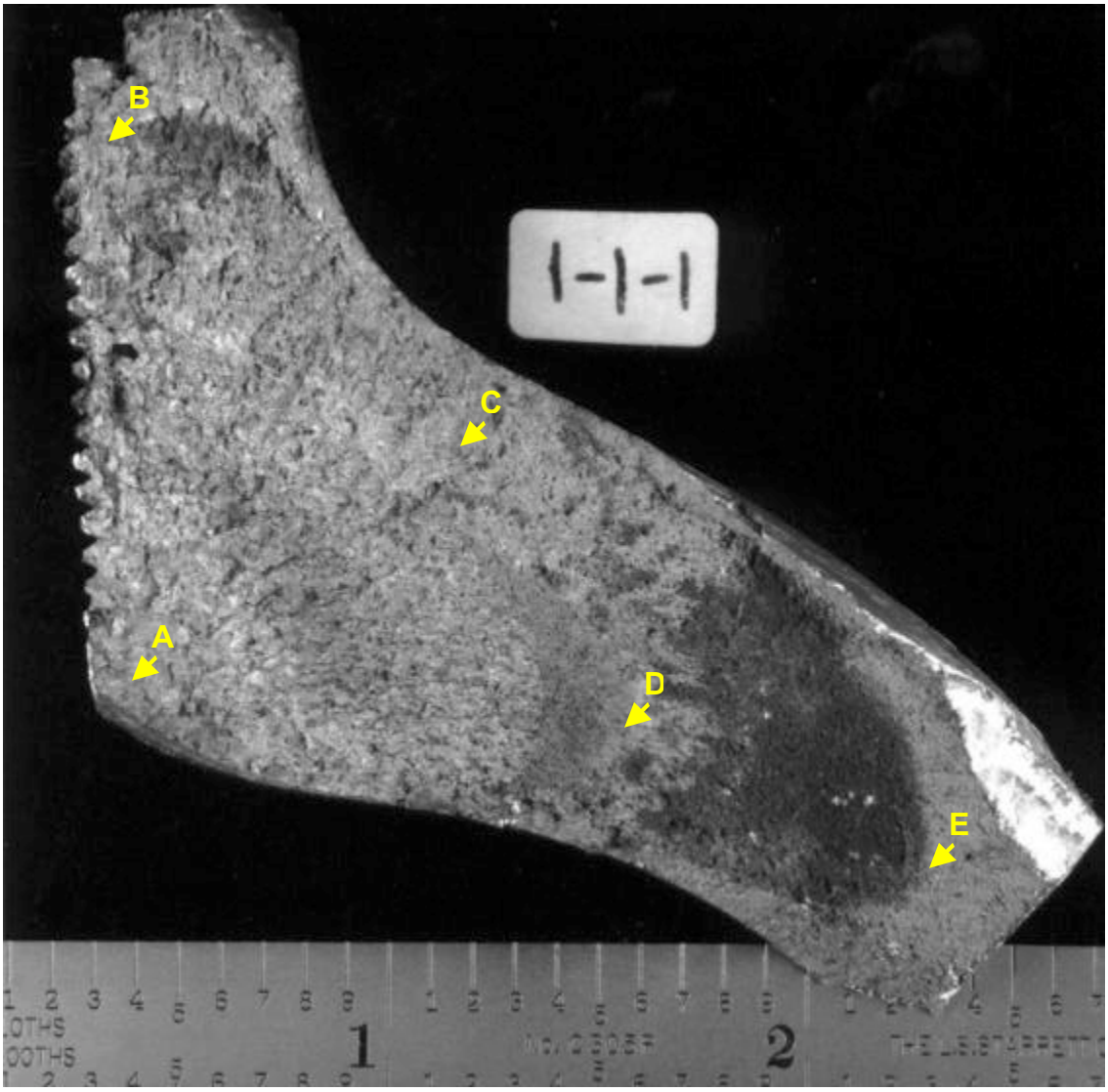

Figure 9. Fractograph of section 1-1-1. Photo ID: DC18344-CEM-3-8/28/00.

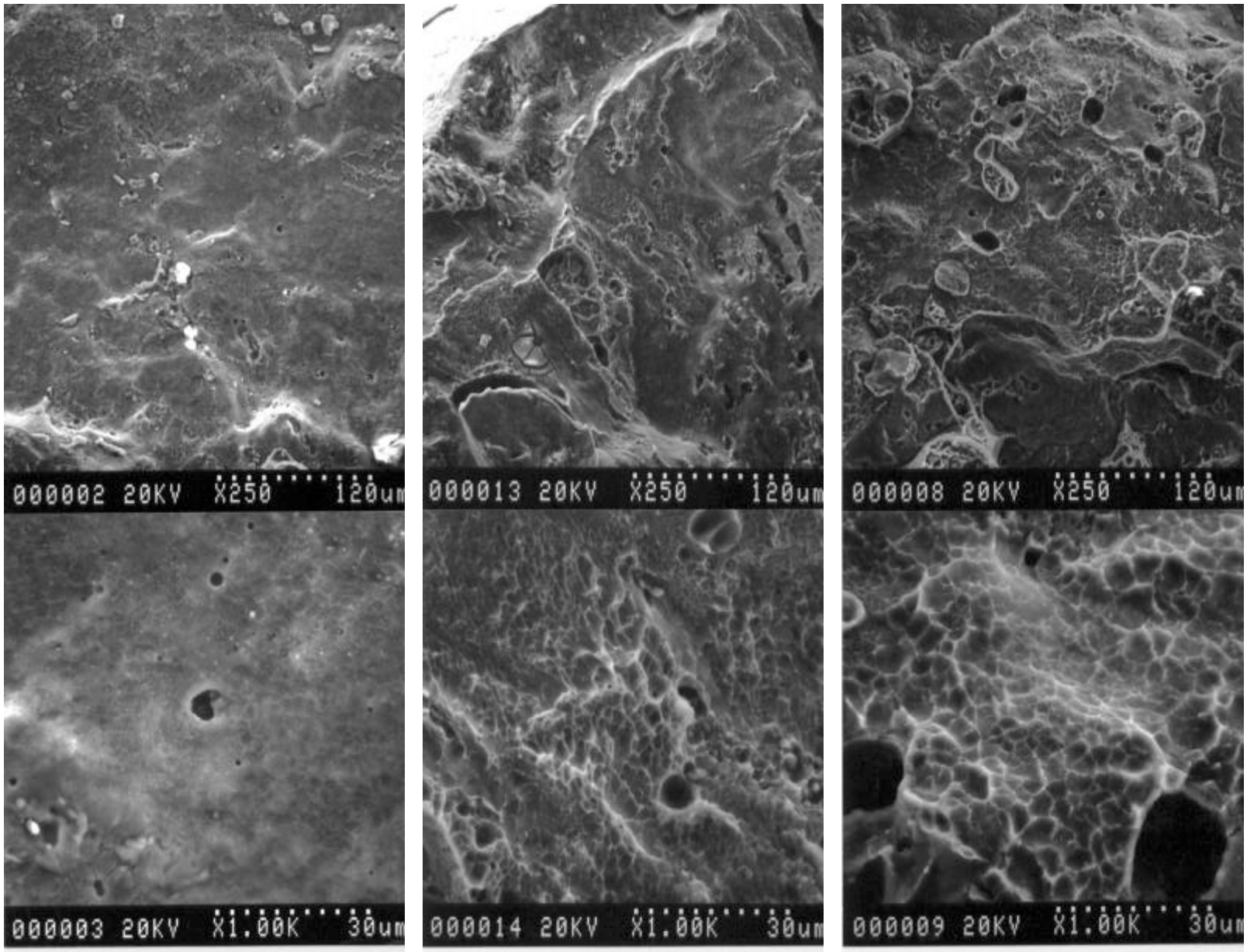

(a) Region A (b) Region B (c) Region C

Figure 10. SEM fractographs from regions shown in Figure 9.

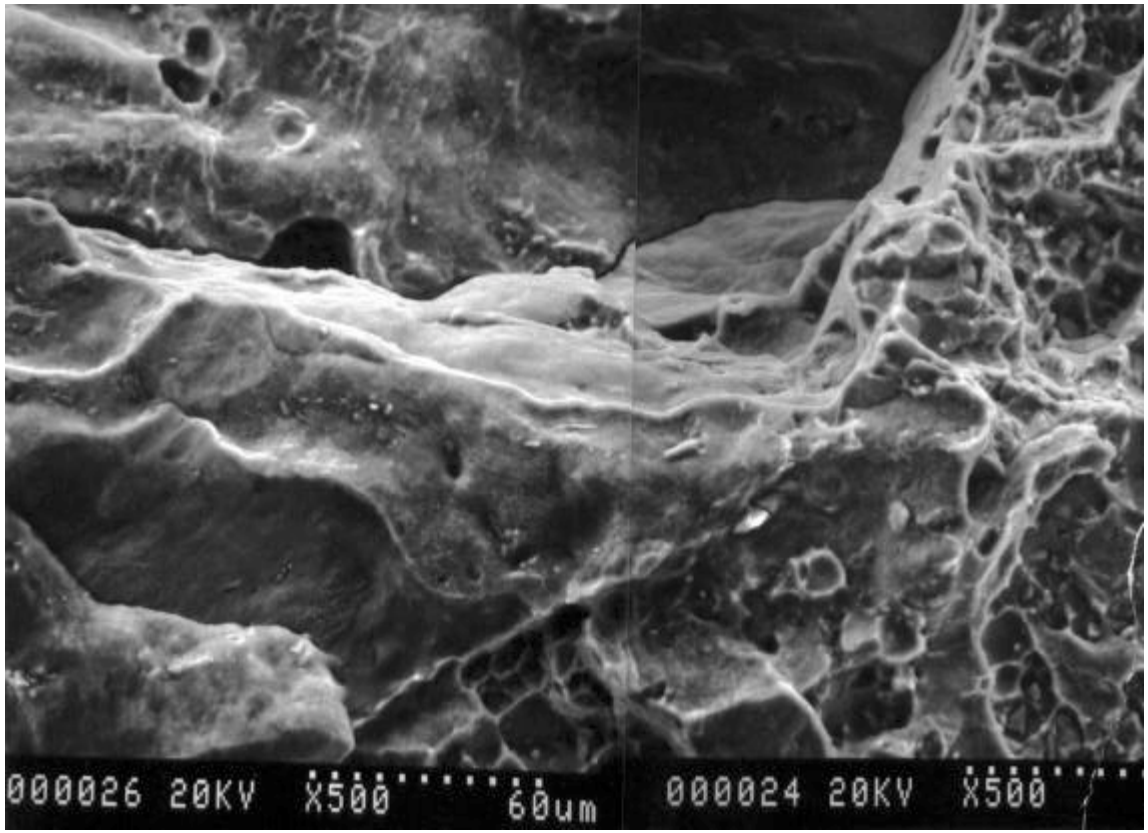

Figure 11. SEM montage from Region D of figure 9. Note the abrupt transition from intergranular fracture with poorly-formed dimples (left) to ductile dimples (right). The fracture progressed from left to right.

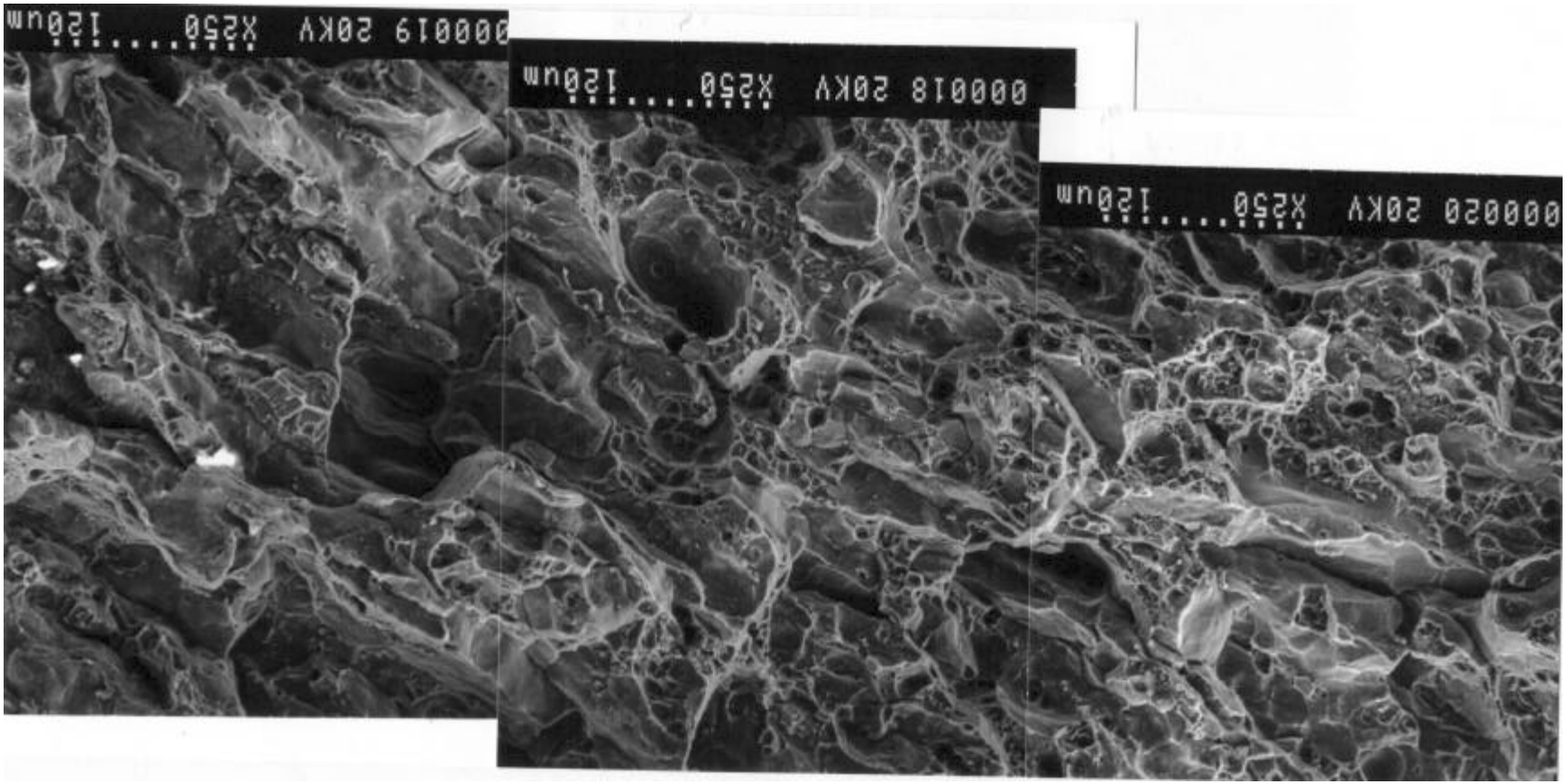

Figure 12. SEM montage from Region E of Figure 9. The fracture progressed from left to right and transitioned in mode from predominantly intergranular fracture with poorly-formed dimples to predominantly ductile rupture.

(a)

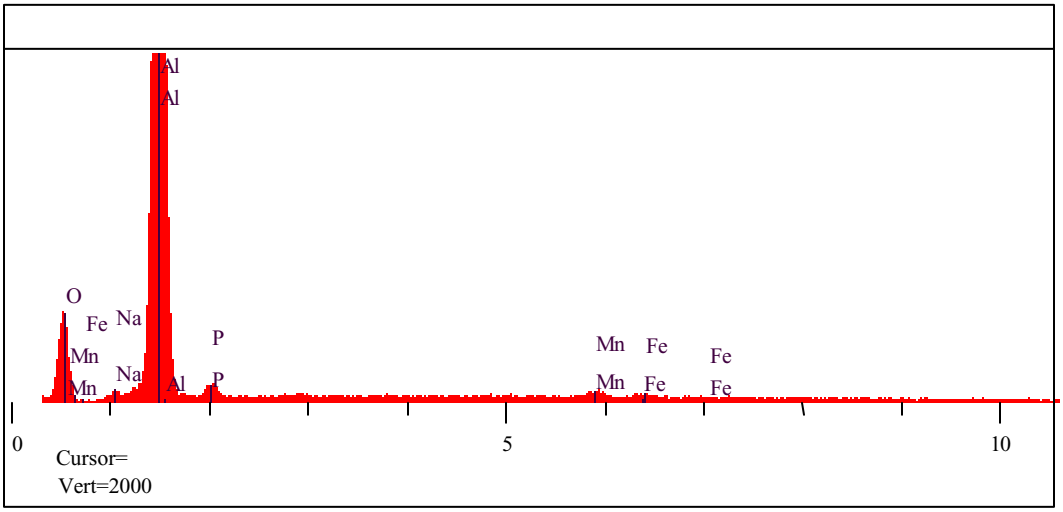

(b)

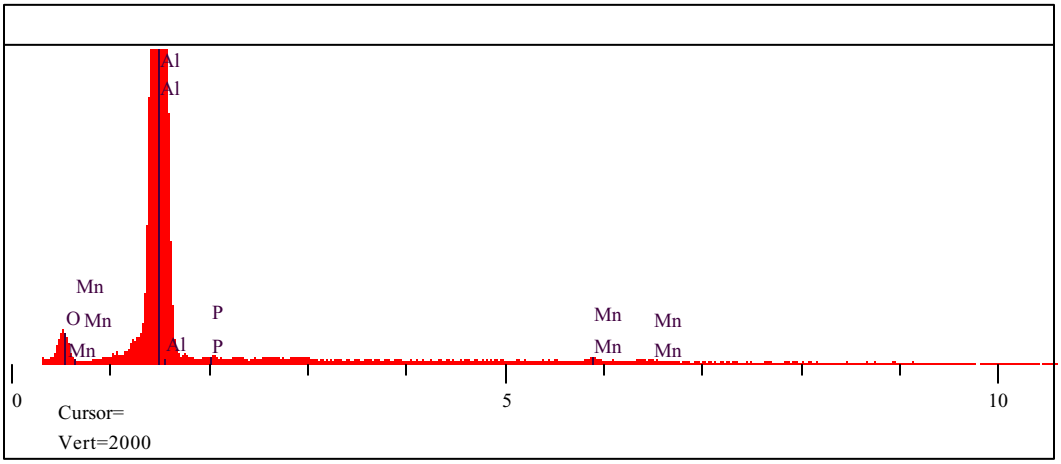

(c)

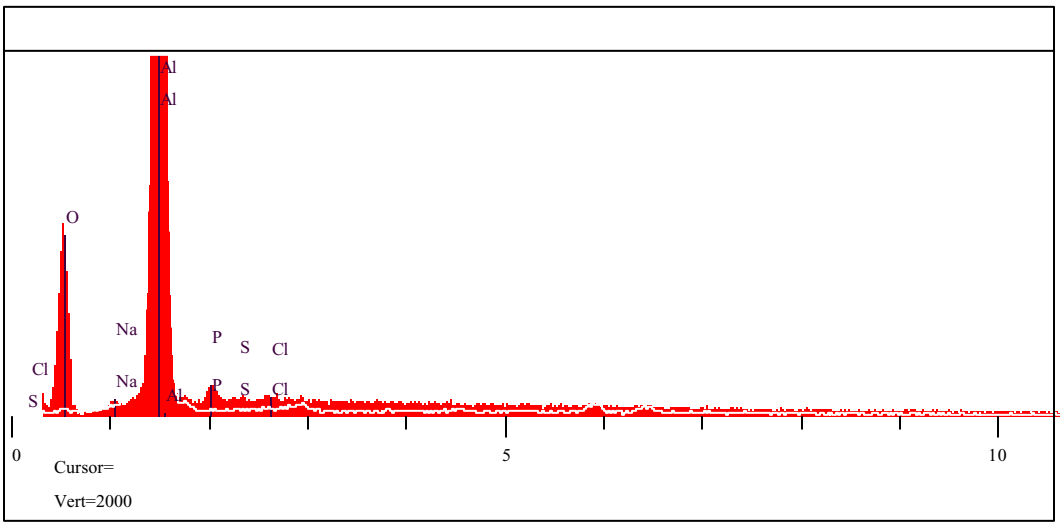

Figure 13. EDS results from 1-1-1 fracture surface.
(a) Region A (b) Region B (c) Region E
Plots show the spectra from the dark area (Figure 9) with the spectrum from the area beyond the beach mark superimposed in white. Note the lack of S, O, Na, Cl and P peaks in the superimposed spectrum.

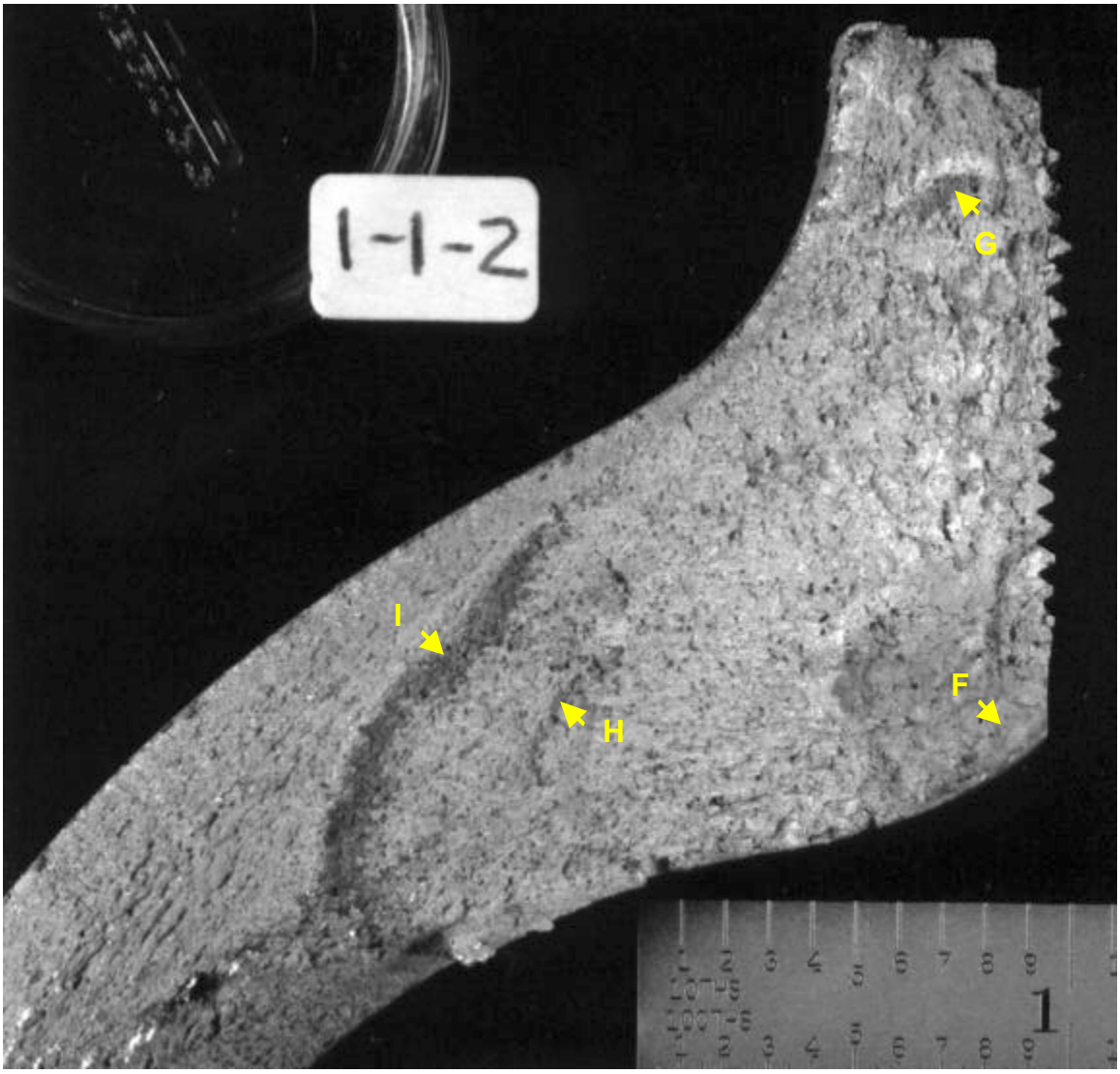

Figure 14. Fractograph of section 1-1-2. Photo ID DC18275-CEM-6-8/28/00

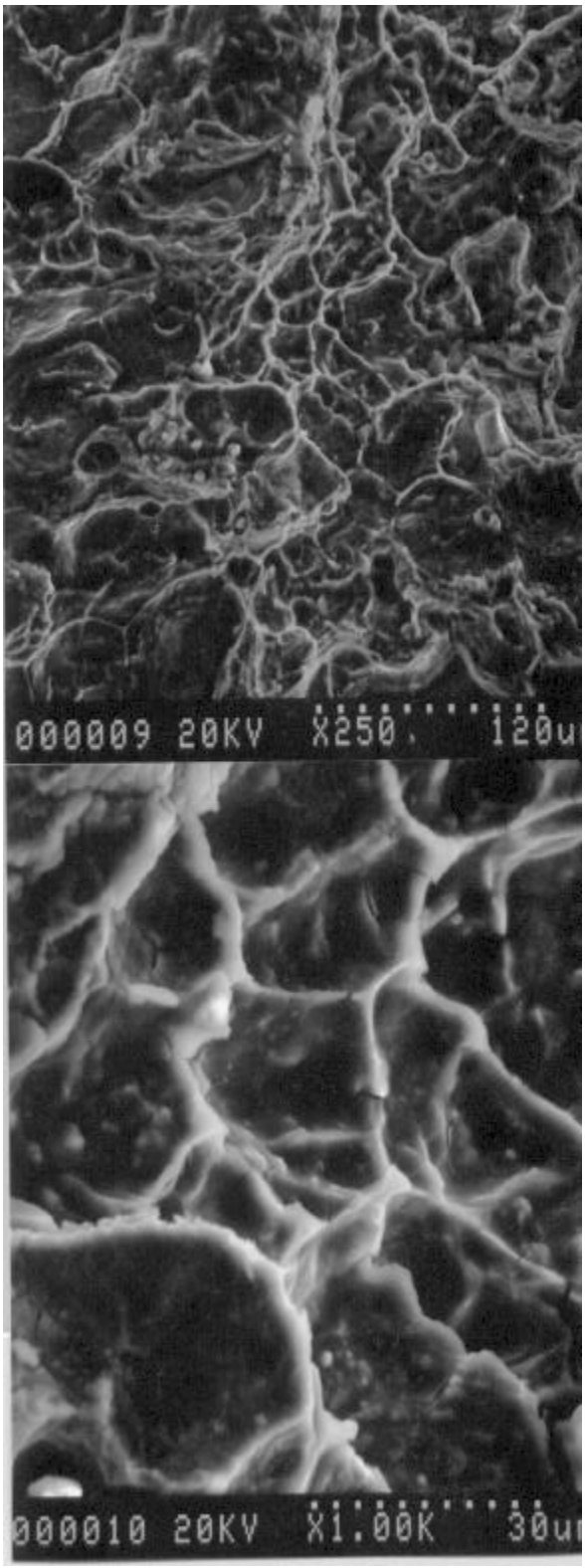

Figure 15. SEM Fractographs from region H on Figure 14.

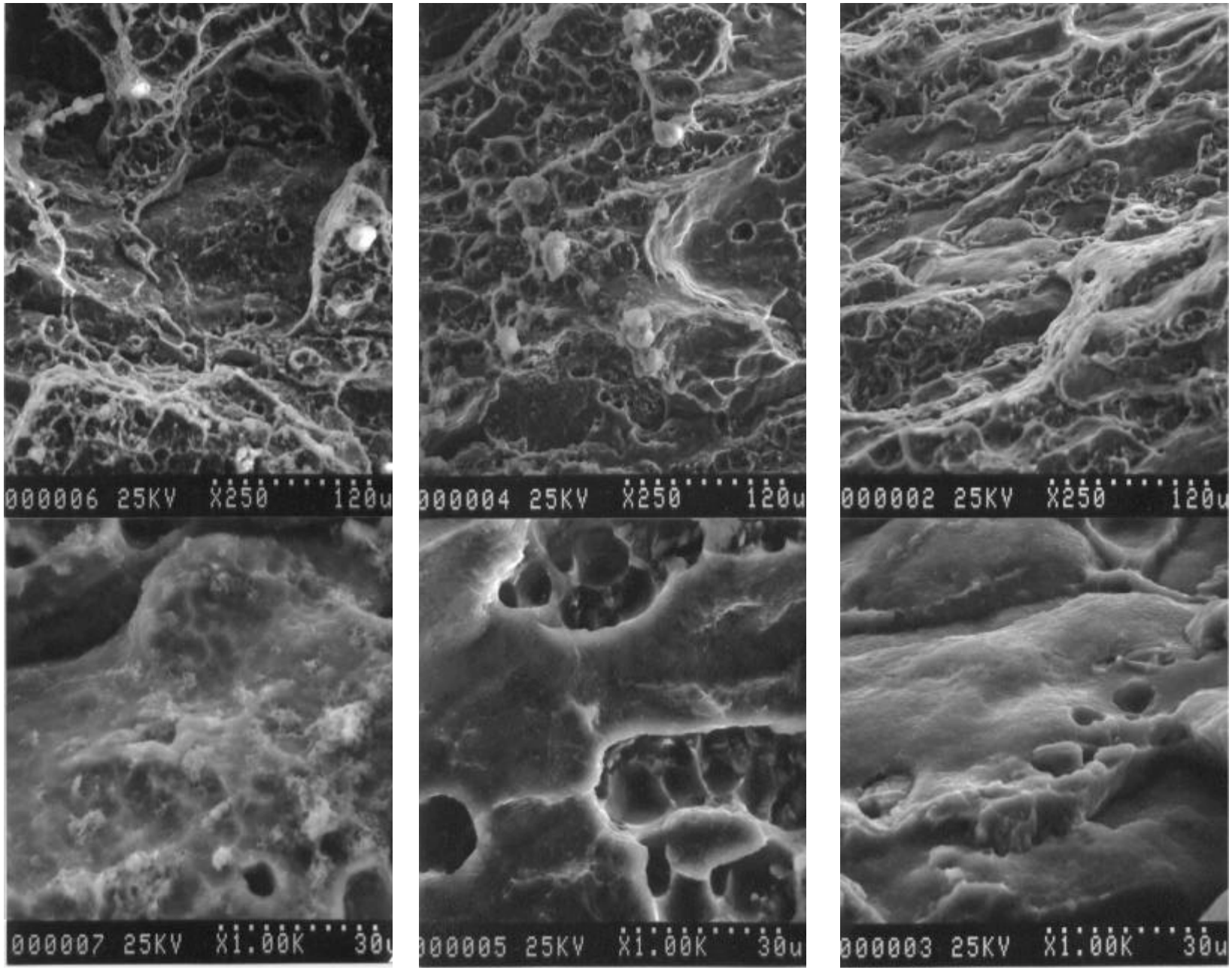

(a) Region I (dark area) (b) Region I (at transition) (c) Region I (beyond transition)

Figure 16. SEM fractographs from regions shown in Figure 14.

(a)

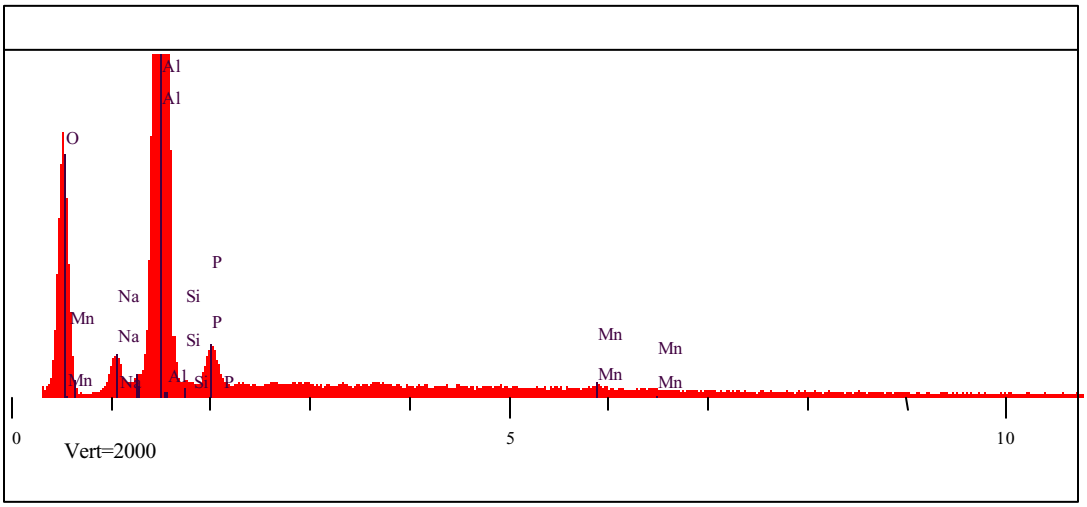

(b)

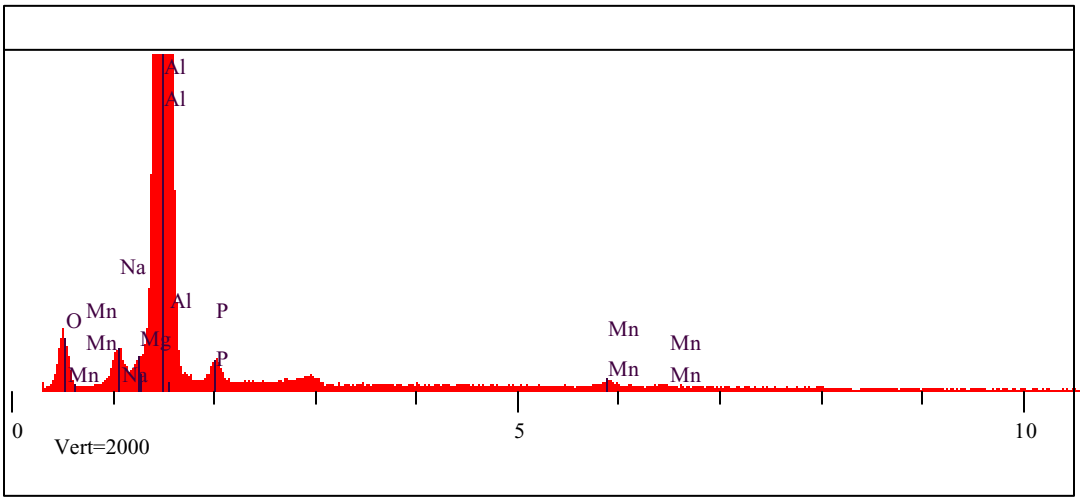

(c)

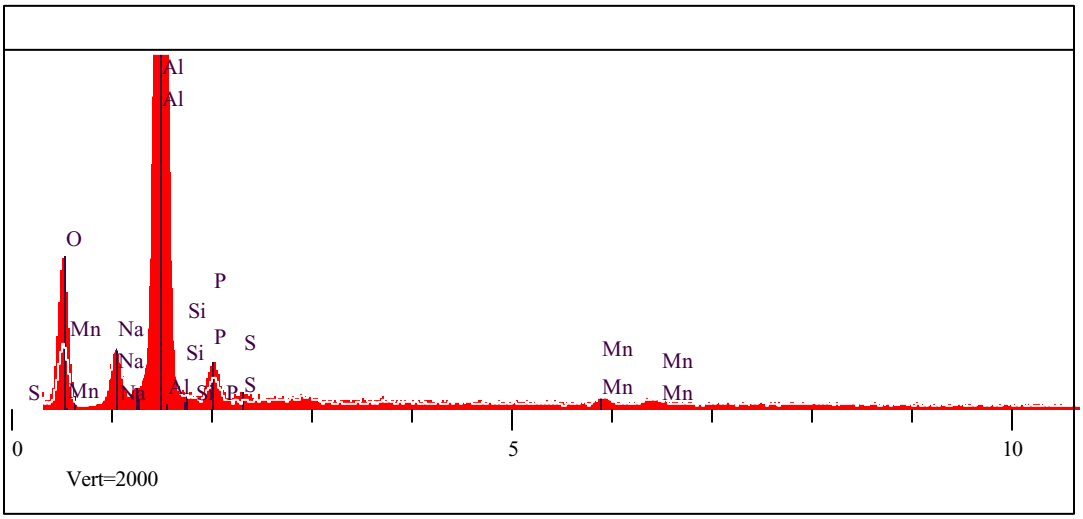

Figure 17: EDS results from 1-1-2 fracture surface.
(a) Region F (b) Region G (c) Region I
Plots show the spectra from the dark area (Figure 14) with the spectrum from the area beyond the beach mark superimposed in white. Note the lower S, O, and P peaks in the superimposed spectrum.

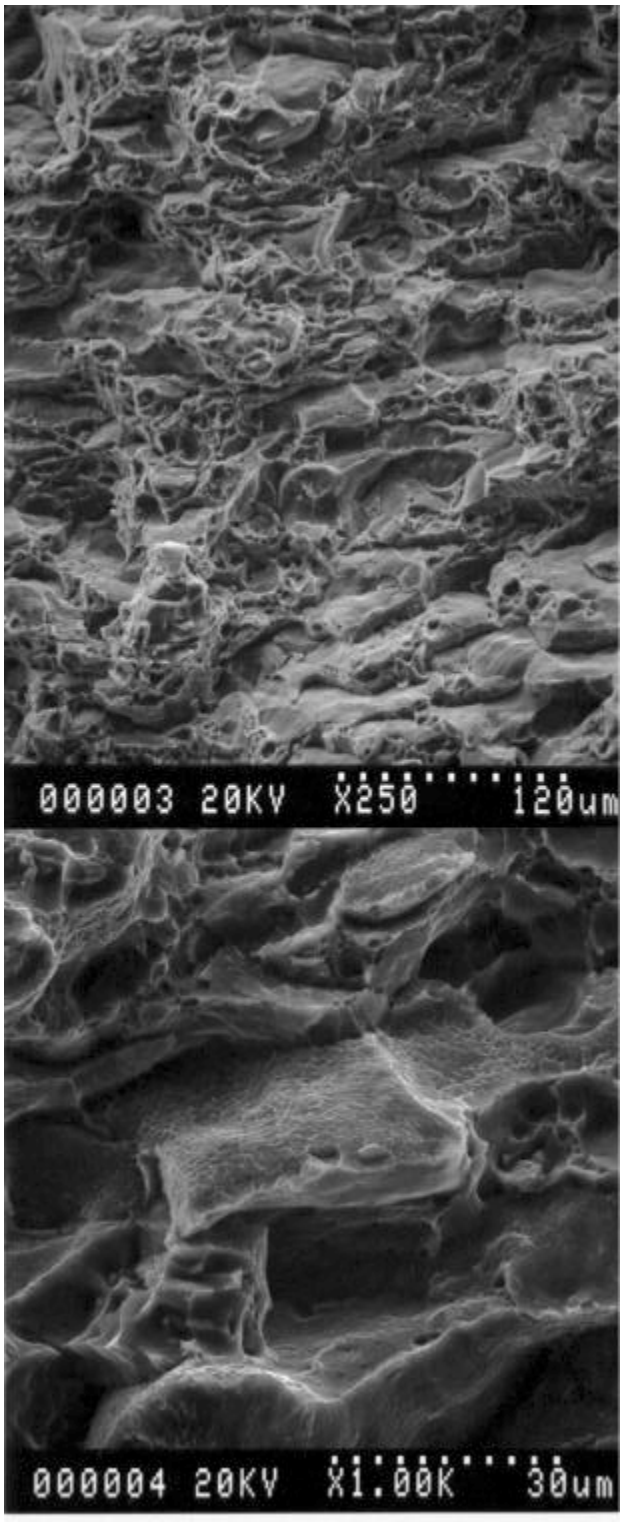

Figure 18. SEM fractographs of tensile specimen 1-2-1.

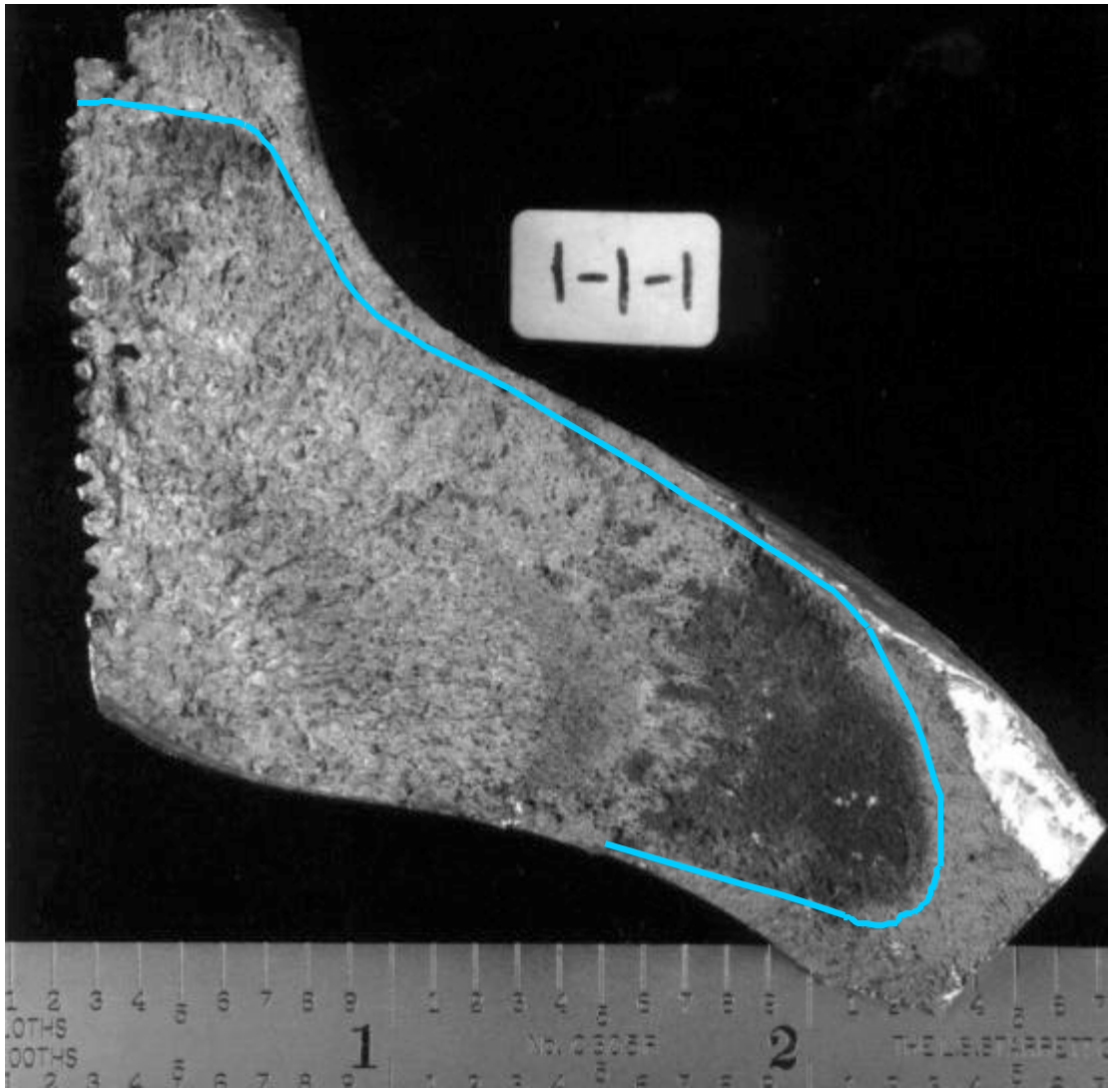

Figure 19: Approximate extent of subcritical crack growth on the 1-1-1 fracture surface.

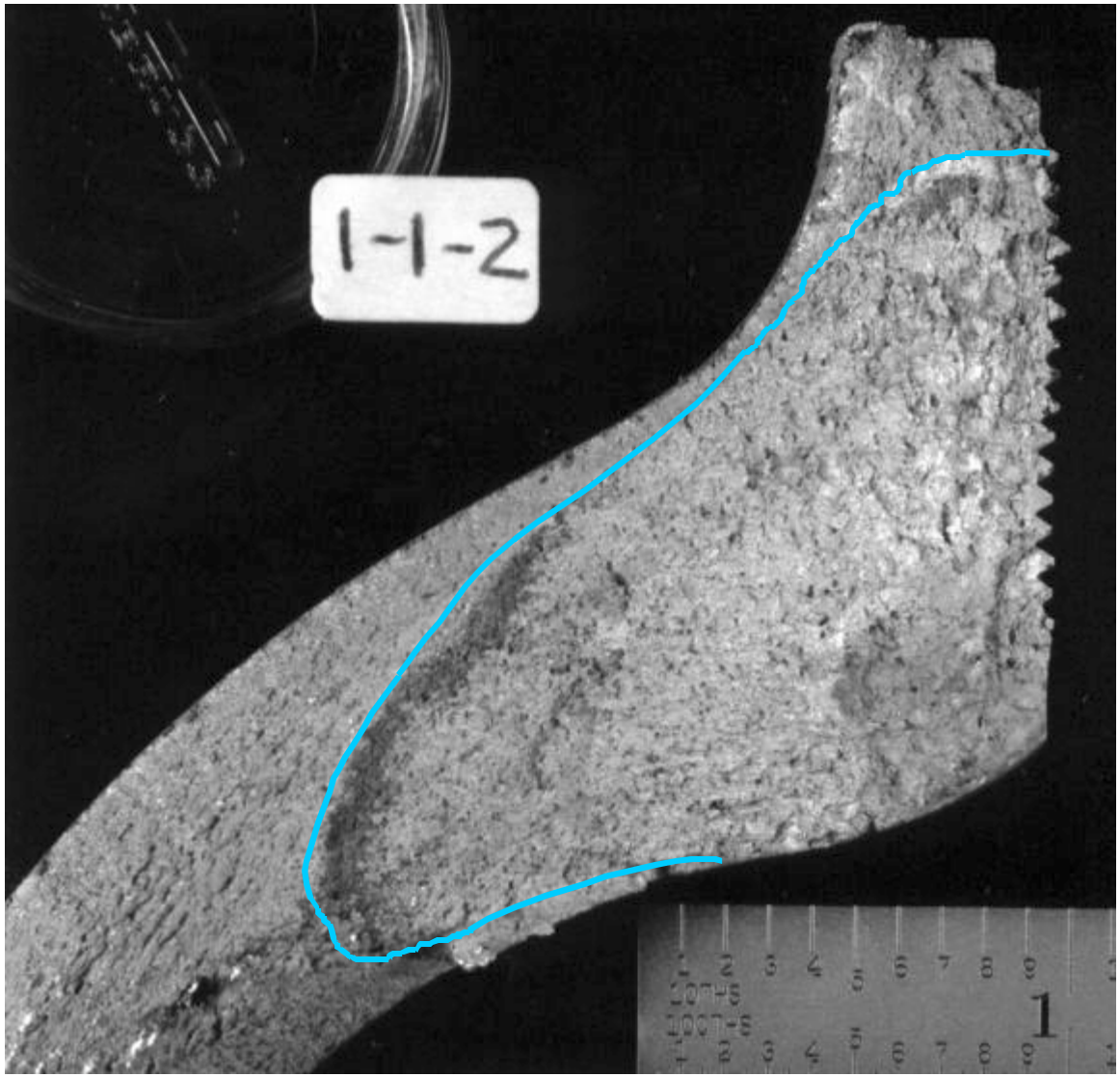

Figure 20: Approximate extent of subcritical crack growth on the 1-1-2 fracture surface.

Appendix A: Recommended Scope of Work

Recommended Scope of Work for Metallurgical Evaluation of Walter Kidde Aluminum SCUBA Cylinder

1. Photodocumentation. Prior to any destructive examination of this cylinder, it will be photodocumented to illustrate its "as-received condition". All stampings on the cylinder will be photodocumented. After each cutting operation needed to remove samples for testing or evaluation (such as required for chemical samples) the cylinder and sample will be photodocumented to illustrate the sample location. Photodocument the primary fracture surface as well as any secondary cracks that may be present. Any corrosion deposits or other visible surface contaminates should also be photodocumented

2. Corrosion. Testing for corrosion product should be done prior to any extensive cutting or handling of the cylinder remains. Swipe samples or cuttings of material containing any such potential corrosion products should be taken. When cutting is performed, care should be used to minimize contamination of the cylinder surfaces. Swipe samples or samples containing potential corrosion products should first be analyzed by scanning electron microscopy and energy dispersive spectroscopy (SEM/EDS).

3. Chemical Analysis. The cylinder aluminum alloy will be analyzed for chemical composition to compare with materials specifications. Material from the neck region, side wall and cylinder bottom will be analyzed to check for alloy homogeneity. The analysis will also determine the concentration of potentially detrimental trace elements, such as lead and bismuth.

4. Macroetching. A thin slice of material will be removed from the neck of the cylinder, including some sidewall material. This slice will be macroetched to show the grain macro/microstructure in this area.

5. Fractography. Fractures will be examined by SEM and stereo-microscopic techniques. Particular attention should be focused in the regions where the fracture originated. Any indications of fatigue, stress-corrosion cracking, ductile rupture, inter/intra-granular fracture features, etc., should be photodocumented.

6. Dimensional Checking. Prior to extensive cutting, the cylinder wall thickness at various locations and other cylinder features, such as threads, cylinder internal diameter, inlet hole diameter should be documented. Measurements done should be sufficient to determine the minimum wall thickness as well as to document any extensive plastic tearing that may have resulted in the failure event.

7. Secondary Cracking. A section of the primary fracture surface near the crack origin should be metallographically polished. Any secondary cracking near the failure origin should be evaluated. These sections should be first examined in the unetched condition and photodocumented to look for crack branching. The sample should then be etched, re-examined and photodocumented.

8. Material Hardness. The material hardness shall be evaluated by means of macrohardness testing according to ASTM standards.

9. Physical Testing.
Mechanical testing will be carried out following the procedure proscribed in 49 CFR, 178.46-13

10. Report. The report should contain a description of all tests performed and the results obtained. If possible, the location of the crack origin, mode of fracture, and likely cause of failure will be stated.

Appendix B: Detailed Photodocumentation of Cylinder

Photo ID: DC18344-R1E8

Photo ID: DC18344-R1E10

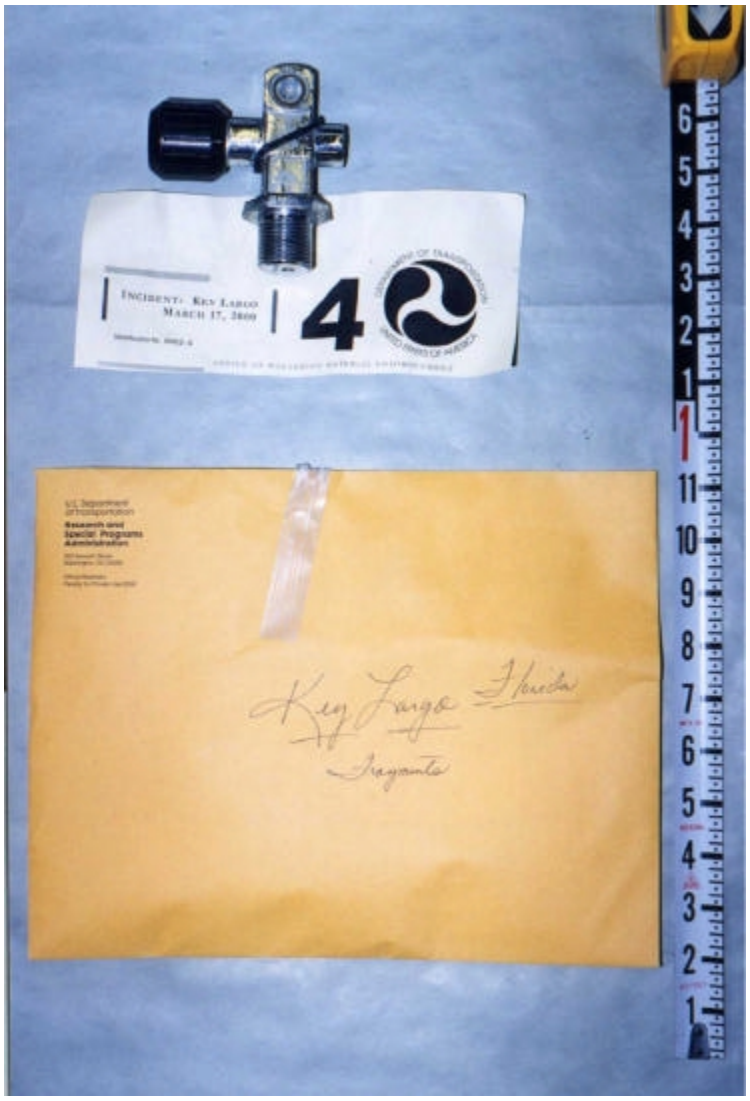

Photo ID: DC18344-R1E12

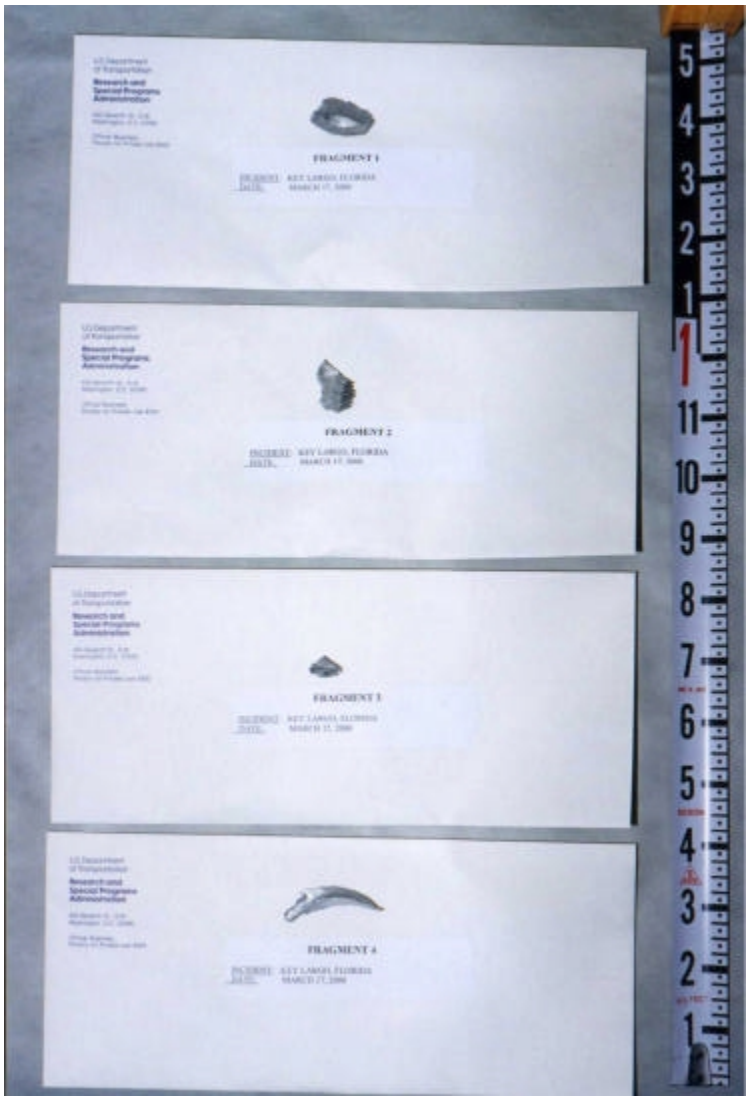

Photo ID: DC18344-R1E15

Photo ID: DC18344-R4E3

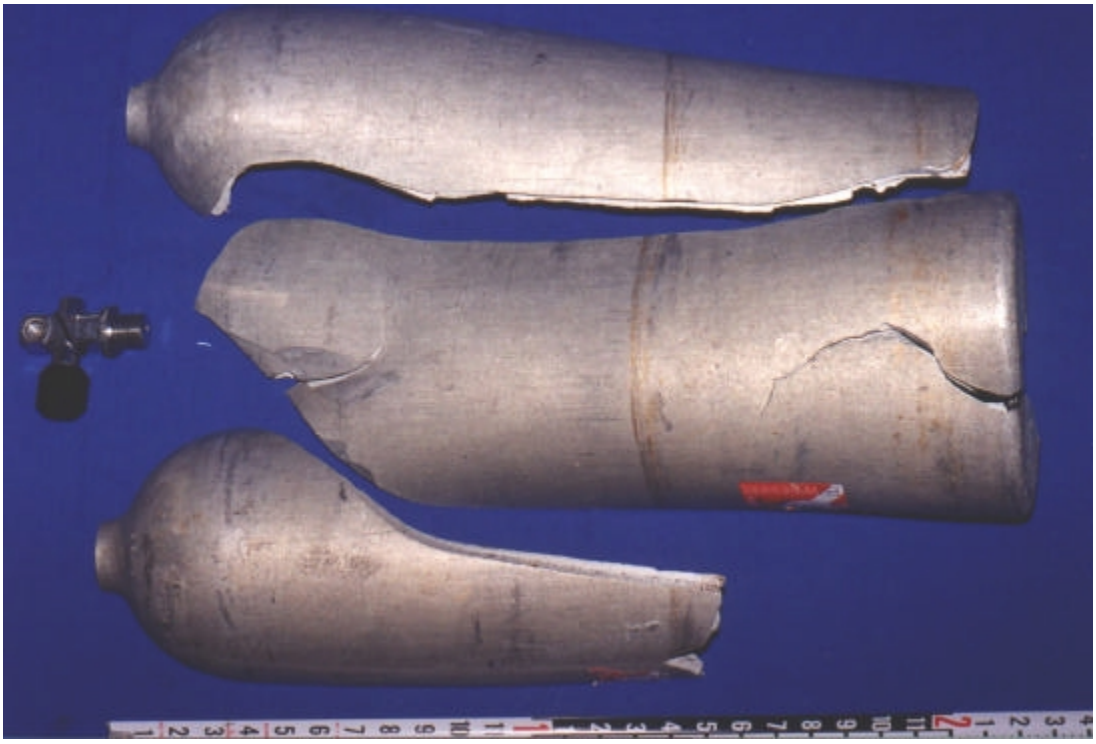

Photo ID: DC18344-R4E6

Photo ID: DC18344-R4E7

Photo ID: DC18344-R4E8

Photo ID: DC18344-R4E9

Photo ID: DC18344-R2E6

Photo ID: DC18344-R4E11

Photo ID: DC18344-R2E8

Photo ID: DC18344-R2E9

Photo ID: DC18344-R2E11

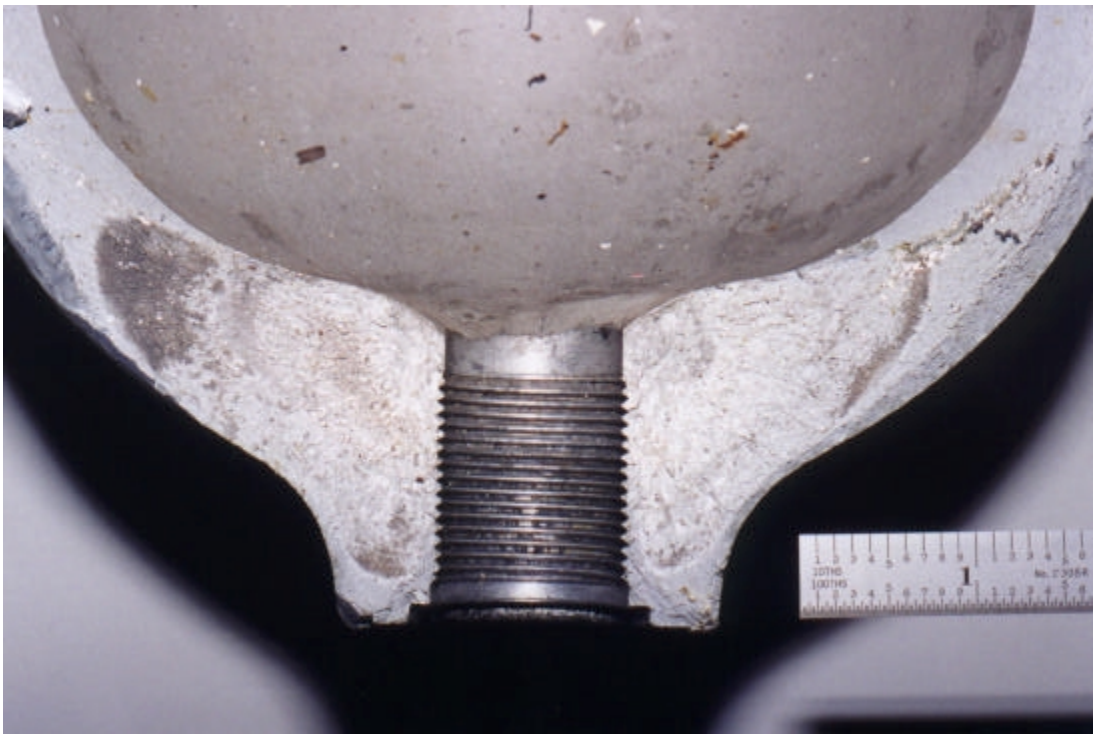

Photo ID: DC18344-R6E13

Photo ID: DC18344-R4E18

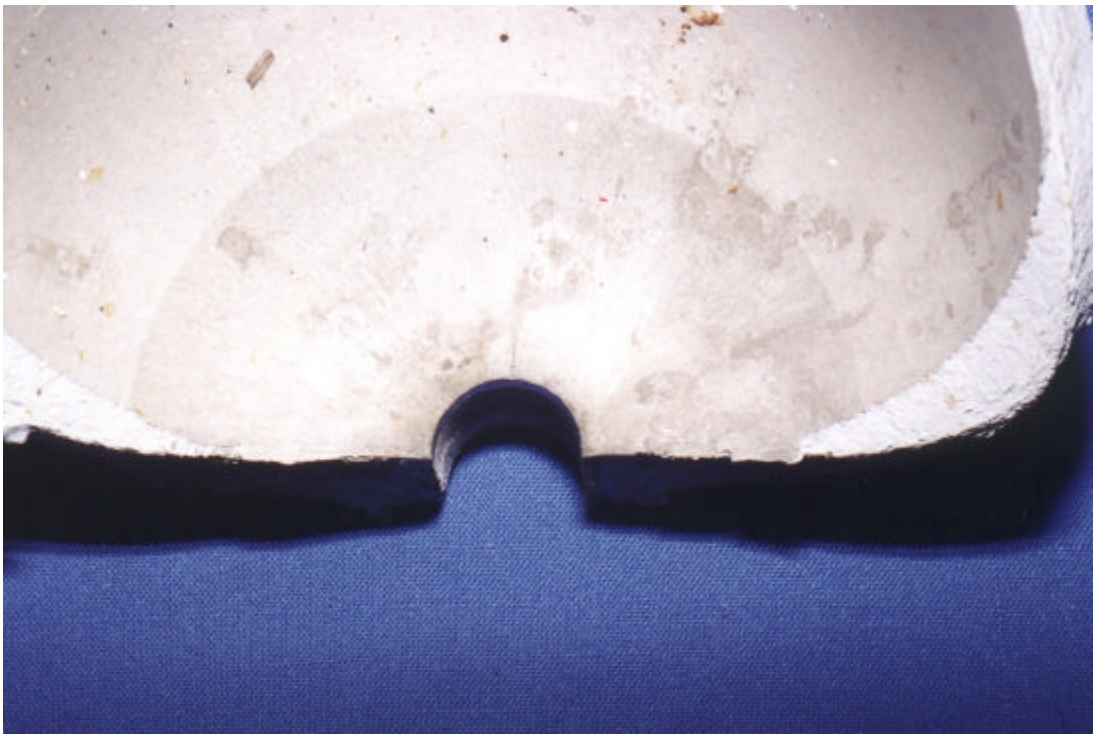

Photo ID: DC18344-R4E19

Photo ID: DC18344-R4E21

Photo ID: DC18344-R6E10

Photo ID: DC18344-R4E23

Photo ID: DC18344-R2E30

Photo ID: DC18344-R2E29

Photo ID: DC18344-R2E28

Photo ID: DC18344-R6E18

Photo ID: DC18344-R5E5

Photo ID: DC18344-R3E4

Photo ID: DC18344-R3E15

Photo ID: DC18344-R3E17

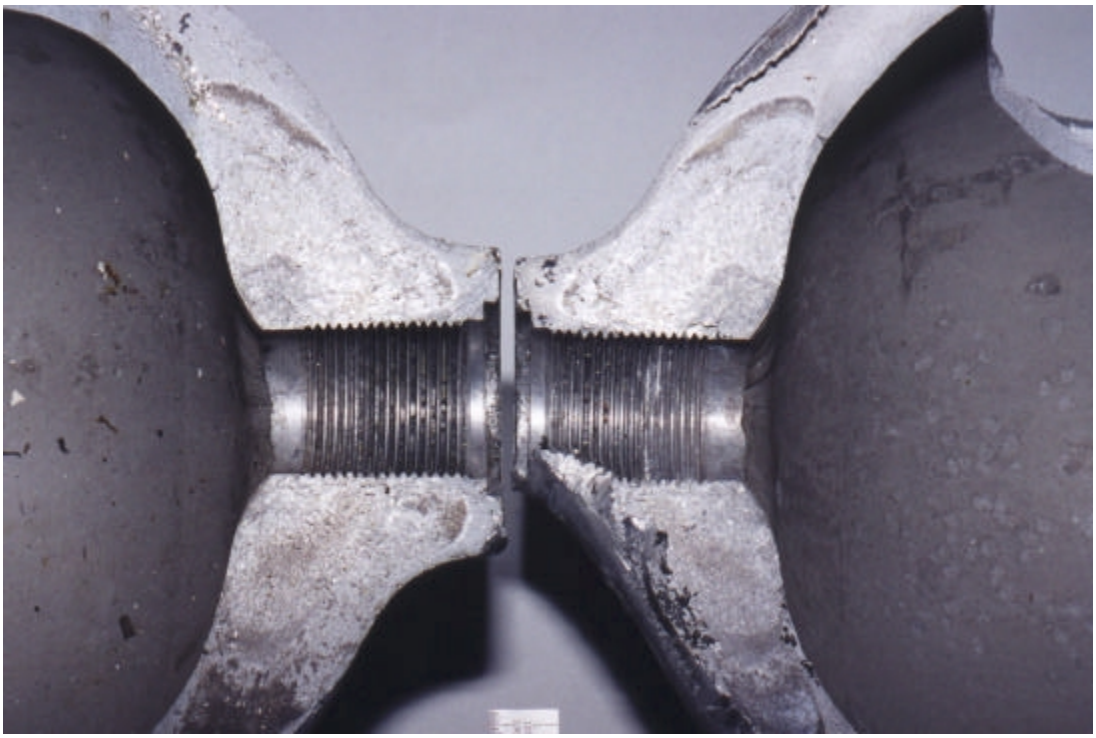

Photo ID: DC18344-R6E23

Photo ID: DC18344-R4E31

Photo ID: DC18344-R4E32

Photo ID: DC18344-R3E23

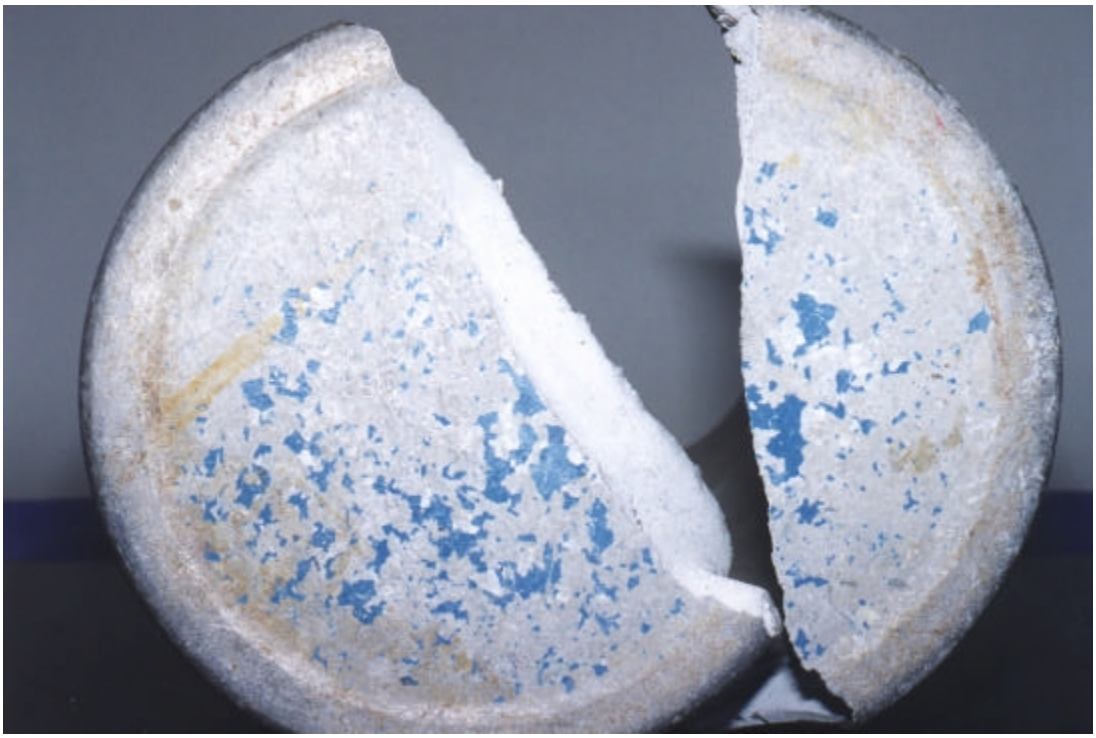

Photo ID: DC18344-R3E21

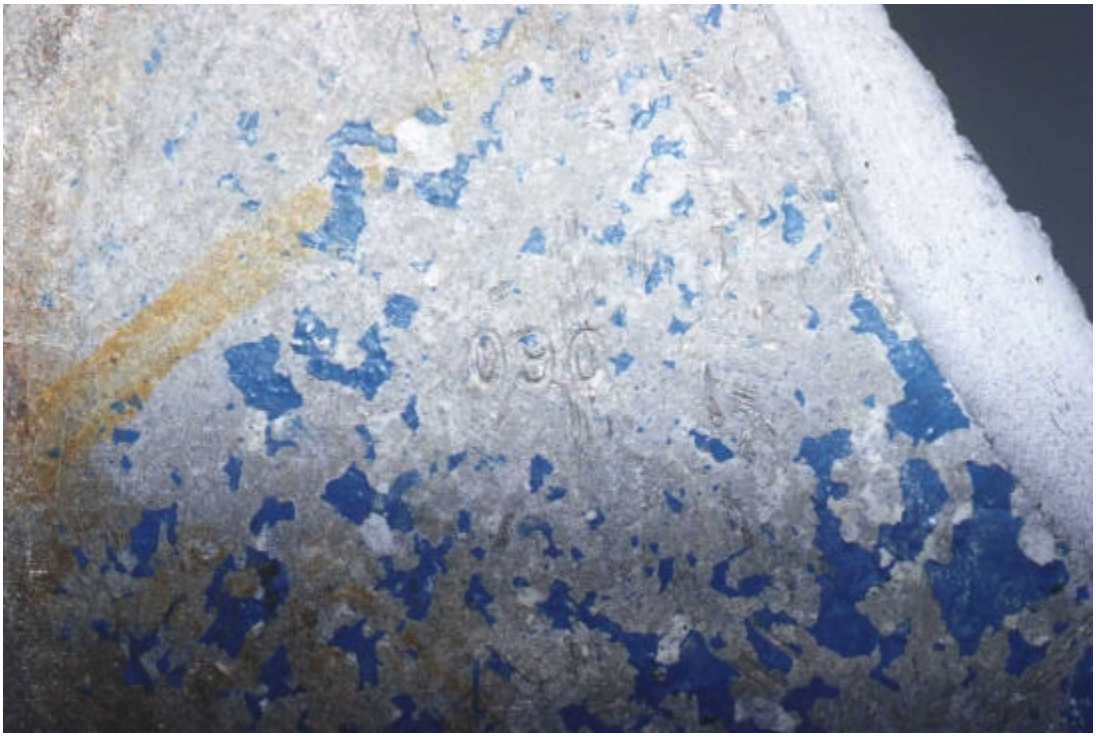

Photo ID: DC18344-R3E22

Photo ID: DC18344-R4E34

Photo ID: DC18344-R3E20

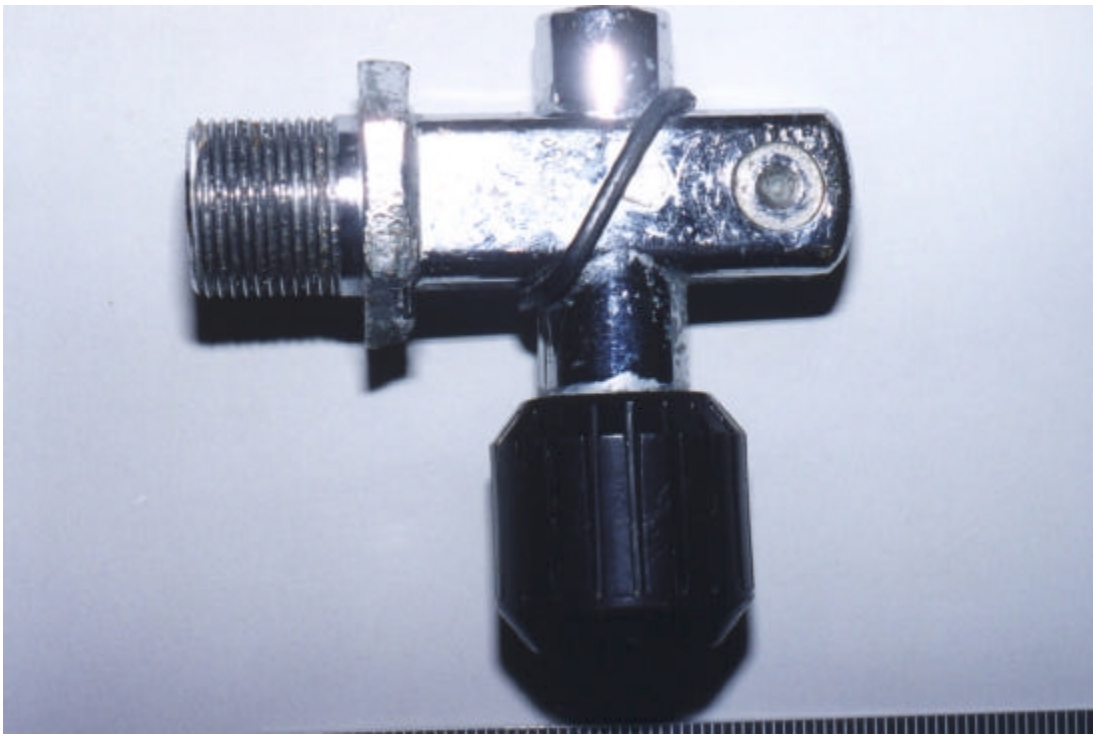

Photo ID: DC18344-R3E28

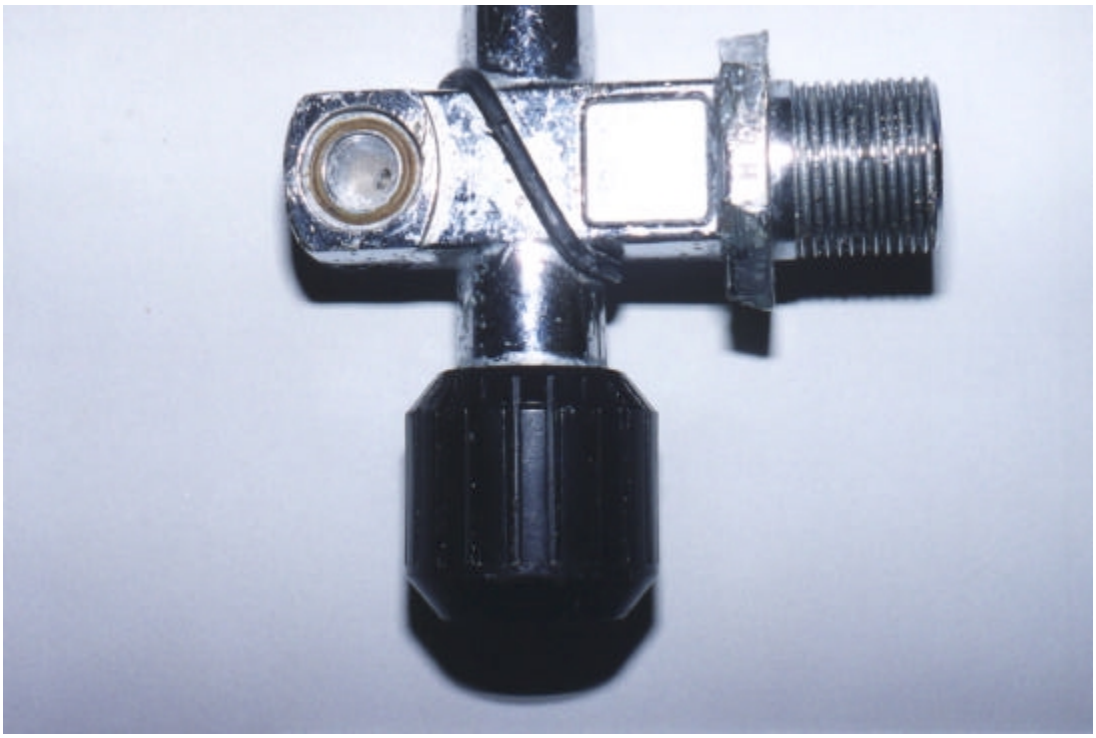

Photo ID: DC18344-R3E29

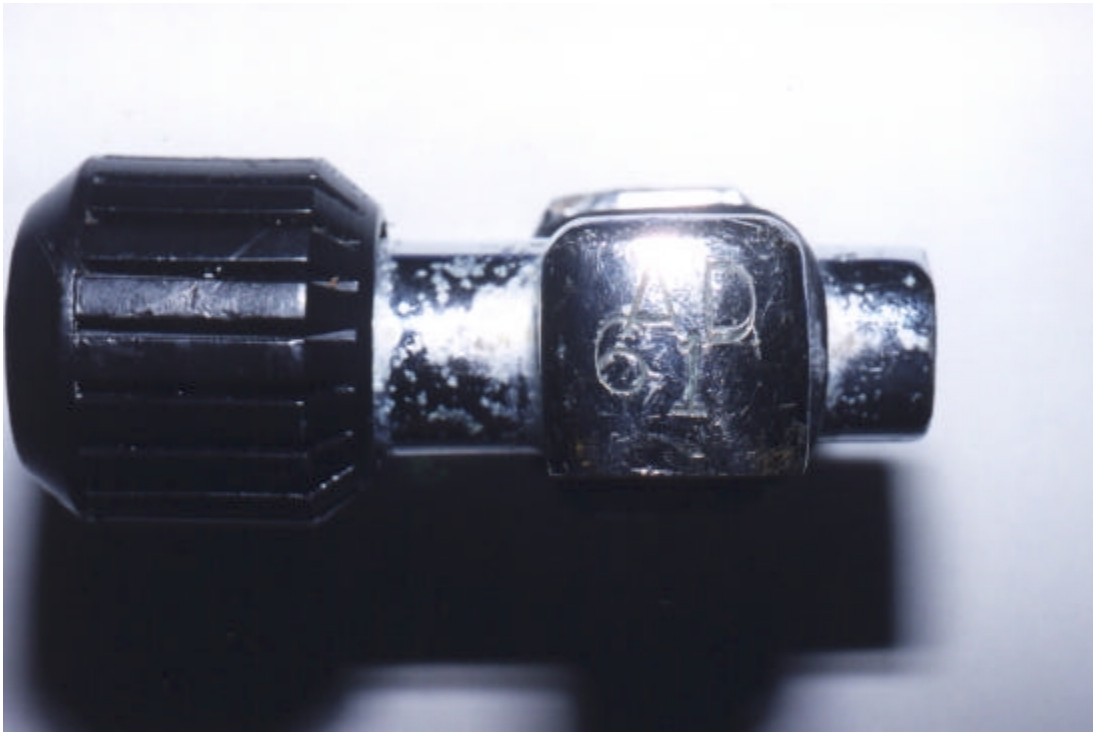

Photo ID: DC18344-R3E31

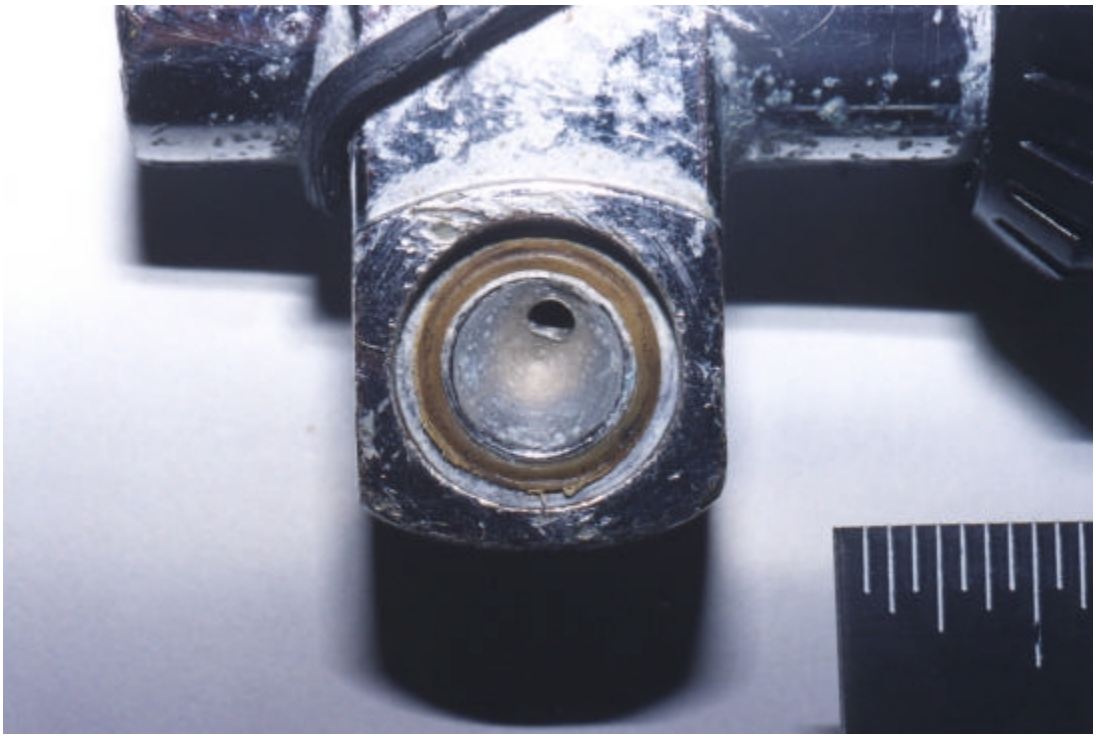

Photo ID: DC18344-R3E32

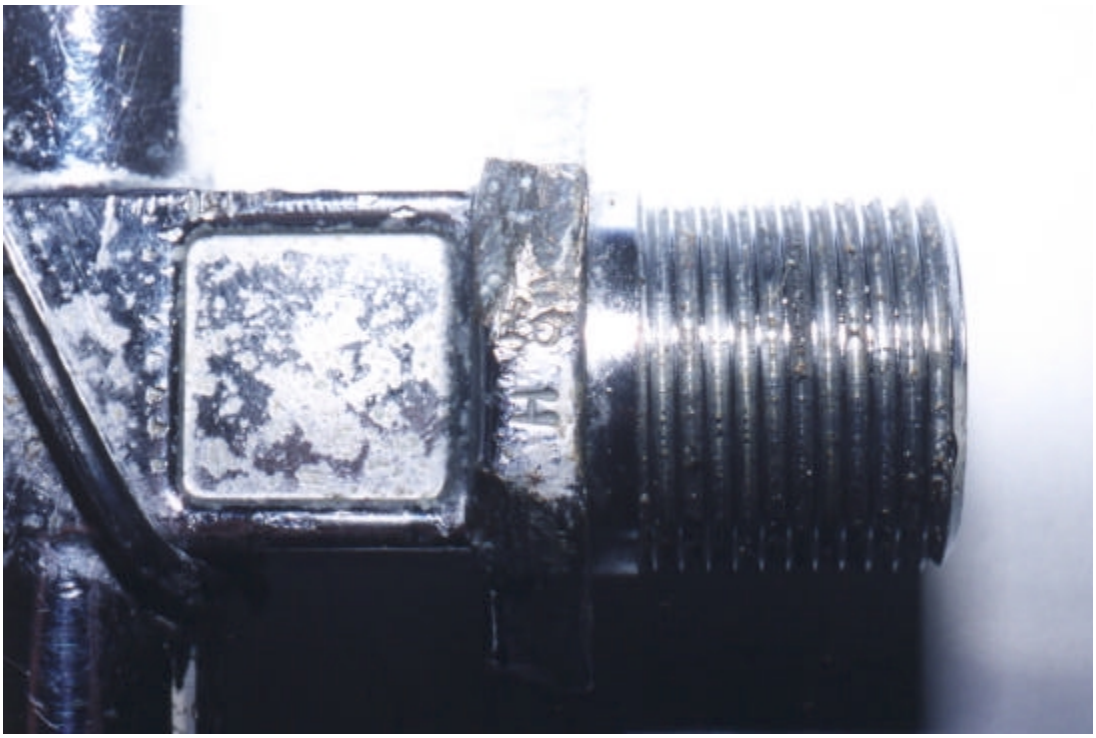

Photo ID: DC18344-R3E33

Photo ID: DC18344-R5E10

Photo ID: DC18344-R5E12

Photo ID: DC18344-R5E14

Photo ID: DC18344-R5E17